Grain size impact on sheet metal behavior via CPFEM

S. Zhou, M. Ben Bettaieb *, F. Abed-Meraim

Université de Lorraine, CNRS, Arts et Métiers Institute of Technology, LEM3, F-57070 Metz, France
DAMAS, Laboratory of Excellence on Design of Alloy Metals for low-mAss Structures, Université de Lorraine, France

A B S T R A C T

A novel multiscale computational framework based on Crystal Plasticity Finite Element (CPFE) modeling is proposed to investigate the effect of grain size on the mechanical behavior and ductility limits of thin metal sheets, featuring both uniform and gradient grain structures. This approach relies on designing unit-cell models that reflect the microstructural characteristics of thin metal sheets. The overall response of the unit cell is obtained from that of its single crystal constituents using the periodic homogenization scheme. At the single crystal level, the mechanical behavior is modeled within a finite strain, rate-independent plasticity framework, where the plastic flow is governed by the classical Schmid law. The effect of individual grain size is incorporated at the single crystal scale by adjusting the critical resolved shear stress (CRSS) evolution, using a combination of the microscopic Hall–Petch relationship and a dislocation density-based hardening model. To efficiently solve the single crystal constitutive equations, a return-mapping algorithm coupled with the Fischer–Burmeister complementarity function is developed and implemented into ABAQUS/Standard through a user-defined material subroutine (UMAT). At the macroscopic level, the ductility limits are predicted by the Rice bifurcation theory. The performance of the proposed strategy is validated through a series of polycrystalline aggregate simulations. The numerical results demonstrate a significant influence of grain size on both the macroscopic strength and ductility limits of polycrystalline aggregates. Additionally, the introduction of gradient grain structures is shown to substantially enhance both strength and ductility. These findings provide valuable insights for optimizing material performance in engineering applications.

1. Introduction

Grain size has a significant influence on macroscopic mechanical properties such as strength, ductility, and toughness [1–9]. Numerous studies have shown that reducing grain size typically enhances yield strength, since small-grain microstructures result in more grain boundaries that act as barriers to dislocation motion [10]. This grain refinement approach has been widely employed in engineering applications to improve material performance, particularly in aerospace, automotive, and biomedical components, where high strength and structural integrity are required. However, while finer grains often enhance strength, they may also lead to significant reduction in ductility. Conversely, coarser grains enhance ductility at the expense of reduced strength. This strength–ductility trade-off is particularly critical in thin metal sheets, where achieving a balance between high strength and adequate formability is essential for applications involving automotive panels, aerospace components, and electronic packaging. Recently, gradient grain structured metals have emerged as promising materials, owing to their superior performance in terms of strength and ductility [11–15]. Understanding the interactions between grain size and mechanical properties is essential for designing and manufacturing high-performance thin metal sheets for advanced engineering applications. This study focuses on the influence of grain size on two main mechanical properties: strength and ductility. Owing to the prohibitive cost of experimental testing, numerical predictive methods have become indispensable for comprehensive investigations of these effects. The development of such predictive tools is intrinsically linked to the adopted constitutive models, which are broadly categorized into macroscopic (phenomenological) models and micro-macro multiscale schemes.

In the earlier investigations, phenomenological models have been used to study the relationship between grain size and yield strength, notably through the seminal works of Hall [16] and Petch [17]. The Hall–Petch relationship, which remains widely applied, correlates the initial yield strength σ_{y0} to the grain size d through the equation:

$$\sigma_{y0} = \sigma_0 + \frac{K_{HP}}{\sqrt{d}}, \tag{1}$$

* Corresponding author at: Université de Lorraine, CNRS, Arts et Métiers Institute of Technology, LEM3, F-57070 Metz, France.
E-mail address: Mohamed.BenBettaieb@ensam.eu (M. Ben Bettaieb).

where K_{HP} is the macroscopic Hall–Petch constant, and σ_0 represents the friction stress opposing dislocation motion. Extensive theoretical and numerical studies have investigated the impact of grain size on strength and ductility. For example, Zuev et al. [18] have analyzed the effect of grain size on flow stress in polycrystalline aluminum samples with grain sizes ranging from 0.008 mm to 5.0 mm. Their findings revealed that flow stress increases as grain size decreases. Xu et al. [19] have further investigated the effect of grain size on ductility limits, coupling the Gurson–Tvergaard–Needleman model [20] and the Thomason model [21] with a surface layer model. The size-dependent component follows the Hall–Petch relationship. Their findings have indicated that the forming limit strain, as predicted by the Thomason coalescence criterion, decreases with the thickness-to-grain size ratio ($= t/d$). Moreover, an increase in strain scatter has been observed when the sheet thickness contained only one or two grains, underscoring the significant role of individual grains in the thickness direction. Additionally, Xu et al. [22] have directly incorporated the size-dependent factor t/d into the Oyane ductile fracture criterion [23], and explored the impact of geometry and grain size on the limit strains determined by uniaxial tensile tests according to Holmberg's method [24]. They found that the predicted limit strains decrease with t/d, a conclusion experimentally confirmed by Wilson et al. [25]. Although phenomenological models exhibit strong predictive capabilities, they often fall short in capturing certain microstructure-related features of material behavior, such as initial crystallographic textures, grain morphology and boundaries, and dislocation dynamics.

To enhance predictions of mechanical behavior and ductility limits in thin metal sheets, several multiscale schemes have been developed. These constitutive frameworks allow for modeling the mechanical behavior at the single crystal level, thus resulting in a refined formulation of the Hall–Petch relationship:

$$\tau_{c0}^{\alpha} = \tau_0 + \frac{\kappa_{HP}}{\sqrt{d}}, \tag{2}$$

where τ_{c0}^{α} denotes the initial critical resolved shear stress (CRSS) for the crystallographic slip system α, τ_0 is the initial CRSS without considering size effects, κ_{HP} represents the microscopic Hall–Petch constant, and d is the grain size. Traditional applications of this relationship often assume an average grain size d over all grains. However, this approach fails to account for grain size variability. In multiscale modeling, the macroscopic mechanical behavior is derived from that of the single crystal constituents using relevant scale-transition schemes. These schemes are typically classified into two categories: mean-field and full-field approaches. One of the most popular mean-field multiscale schemes is the Taylor model. Despite its popularity and wide use, the Taylor model has significant limitations, including its inability to satisfy equilibrium at the grain level and its inadequate representation of grain morphology and interactions with surrounding grains. To overcome these issues, the mean-field self-consistent approach has been introduced, which fulfills equilibrium at the polycrystalline scale and better accounts for grain morphology by modeling grains as ellipsoids. In this field, Berbenni et al. [26] have explored grain size effect on macroscopic yield stress by integrating the Hall–Petch relationship into an elastic-viscoplastic self-consistent model. Nicaise et al. [27] have extended this model to include the effect of grain size distribution and crystallographic texture, showing that grain size dispersion reduces macroscopic yield stress with a significant impact comparable to crystallographic orientation. Additionally, Franz et al. [28] have used the Rice bifurcation criterion in conjunction with the Kocks dislocation density-based hardening model [29] to address size effects, finding that ductility limits decrease as grain size diminishes. Despite these advances, mean-field approaches remain limited in accurately modeling polycrystalline behavior and predicting ductility limits, particularly in materials with complex microstructures. They are also unable to predict the local strain and stress fields within individual grains, which can lead to significant fluctuations in local mechanical variables for strongly anisotropic materials. Additionally, mean-field schemes cannot adequately account for the effects of real grain shapes as well as grain spatial distribution. As a result, full-field multiscale schemes have been developed to more accurately capture microstructural features, such as real grain morphology and boundaries. These full-field approaches, based on Crystal Plasticity Finite Element Method (CPFEM) [8,30–42] or Crystal Plasticity Fast Fourier Transform (CPFFT) [43–46], often use periodic boundary conditions (PBCs) to account for spatial variation of strain fields within the microstructure. Recent studies have successfully incorporated the microscopic Hall–Petch relationship into full-field multiscale schemes, significantly improving predictions of the mechanical behavior of polycrystalline materials. Notable contributions include work by [47–53], who have demonstrated the effectiveness of these approaches in combination with phenomenological hardening models at the single crystal scale to enhance predictions of mechanical behavior and ductility limits of polycrystalline aggregates. Lakshmanan et al. [54] have integrated the microscopic Hall–Petch equation into the PRISMS-Plasticity software to study the effects of texture and grain morphology on yield strength, plastic stress–strain response, and the Hall–Petch slope in magnesium alloys. Their results show that these properties are highly dependent on texture and grain morphology. More recently, Zhou et al. [39] have incorporated the microscopic Hall–Petch relationship into a rate-independent crystal plasticity model to predict the mechanical behavior and ductility limits of thin metal sheets, demonstrating significant impact of grain size on these properties. Additionally, they showed that grain boundaries can lead to the formation of dislocation pile-ups, thereby increasing the CRSS necessary to move dislocations. Furthermore, grain boundaries play a crucial role in accurately predicting mechanical behavior. In this regard, Chandra et al. [55,56] have analyzed the effect of grain size on mechanical behavior of Ni-based alloy 690 by explicitly modeling finite thickness grain boundaries within the crystal plasticity framework. Li et al. [57] have introduced an explicit grain boundary affected zone (GBAZ) model, which correlates the strength of this region with its proximity to the grain boundary. This model effectively predicts grain size dependence of mechanical properties in polycrystalline materials, but has limitations in capturing the anisotropy of grain boundary deformation.

Strain gradient crystal plasticity (SGCP) is a widely-used approach for studying size effects [46,58–63]. This approach introduces a length scale associated with plastic strain gradients into the constitutive model, where the strain gradients are induced by Geometrically Necessary Dislocations (GNDs). Haouala et al. [46] have investigated the impact of grain size on flow stress using an SGCP model combined with the FFT homogenization technique, concluding that simulations tend to overestimate flow stress for smaller grains and larger strains due to continuous GND accumulation at grain boundaries, which is not compensated by annihilation of dislocations through dynamic recovery. Jiang et al. [58] have proposed a new approach based on surface GND density to investigate grain size effects, demonstrating that the classic Hall–Petch effect can be reproduced. Their findings showed that approximately 80% of dislocation density is stored in the fine regions near grain boundaries at low strain. Zhang et al. [60] and Liu et al. [62] have used an SGCP model to predict the mechanical behavior of gradient-structured metals under various loading conditions. Their investigations have revealed that the SGCP approach is able to capture size effects, with smaller grain sizes leading to higher GND density. However, the application and validation of the Rice bifurcation analysis within a non-local SGCP framework are still matters of ongoing research.

In this work, a size-dependent CPFE-based multiscale computational strategy is developed to investigate the influence of grain size on the strength and ductility limits of thin metal sheets. To achieve this, the microscopic Hall–Petch relationship is incorporated into a finite strain, rate-independent crystal plasticity framework by explicitly accounting for the individual grain size. Unlike previous approaches that use an average grain size, this model enables a more accurate representation of local grain size effects, offering deeper insight into their influence on mechanical behavior and ductility limits. To solve the single crystal constitutive equations, a return-mapping algorithm combined with the Fischer–Burmeister complementarity function is implemented. This approach merges two essential tasks: identifying the set of active slip systems, and determining their slip rates. This combined approach enhances efficiency and robustness, significantly reducing CPU time compared to the traditional return-mapping algorithm, as demonstrated by [64]. In contrast to many earlier studies based on rate-dependent formulations at the single crystal scale, the use of a rate-independent model in this work enables the application of bifurcation analysis. Within rate-dependent formulations, the smoothness of the yield surface prevents accurate bifurcation detection, often requiring the introduction of artificial imperfections. A polycrystalline unit cell, designed and generated using the Voronoi tessellation technique, is used to represent the material microstructure. Additionally, the periodic homogenization technique, which applies periodic boundary conditions (PBCs), is adopted to determine the overall mechanical behavior. Numerous prior studies (such as, [65]) have demonstrated that PBCs offer a more precise prediction of microscopic fields, subsequently leading to a more reliable estimation of the macroscopic response. The Rice bifurcation theory is employed to predict the onset of localized necking at the macroscopic level. Unlike the initial imperfection analysis (M–K approach), the Rice bifurcation approach does not necessitate parameter fitting. Also, when the M–K approach is used, the ductility limit prediction strongly depends on an initial imperfection factor f_0. Furthermore, adopting the bifurcation theory significantly reduces the required CPU time for limit strain predictions. Numerical simulations are performed on unit cells with uniform grain structures, varying grain sizes and thicknesses, to assess the size effects on initial macroscopic yield strength, and hence macroscopic mechanical behavior. Additionally, the influence of initial dislocation density and loading strain paths is also explored. It is well known that coarse-grained materials typically exhibit higher ductility, but lower yield strength. By contrast, grain refinement improves yield strength, but often leads to a significant reduction in ductility. To address this strength–ductility trade-off, a gradient grain structure model with random grain morphology is introduced, unlike prior studies assuming cubic grain morphology [60,62]. Then, the effect of various gradient grain structures on macroscopic strength is investigated. Furthermore, the macroscopic strength and ductility limits of uniform and gradient grain structures are compared, and the trade-off between strength and ductility is ultimately analyzed.

The remainder of this paper is organized as follows. Section 2 describes the proposed CPFE-based multiscale computational strategy, periodic homogenization equations and size-dependent single crystal constitutive equations, as well as the corresponding integration algorithm. Furthermore, the Rice bifurcation criterion is briefly introduced. In Section 3, the simulation results are presented. The size effects on the strength and ductility limits of thin metal sheets with uniform and gradient grain structures are extensively discussed. Additionally, the strength and ductility limit trade-off is analyzed. The conclusions of the present work are given in Section 4.

Conventions and notations

Microscopic (resp. macroscopic) variables are designed by lowercase (resp. capital) letters.
Vectors and tensors are denoted by **bold** letters or symbols.
Scalar parameters and variables are represented by thin and *italic* letters or symbols.

$\vec{\bullet}$	vector.
$\dot{\bullet}$	time derivative of $\bullet$.
$\bullet^{-1}$	inverse of $\bullet$.
$\bullet^{T}$	transpose of tensor $\bullet$.
$\bullet \cdot \bullet$	simple contraction or contraction on one index (inner product).
$\bullet : \bullet$	double contraction or contraction on two indices (inner product).
$\bullet \otimes \bullet$	tensorial product (external product).
$\delta^{\alpha\beta}$	Kronecker delta.
$\bar{\bullet}$	tensors and vectors expressed in the lattice frame.

2. Theoretical framework

This section describes the proposed CPFE-based multiscale computational strategy, including the periodic homogenization equations, the size-dependent single crystal constitutive equations, and the associated integration algorithm. In addition, the Rice bifurcation criterion is briefly introduced.

2.1. Development of the size-dependent CPFE-based computational strategy

In this work, we introduce a novel Crystal Plasticity Finite Element (CPFE)-based computational strategy specifically designed to efficiently predict size effects in thin metal sheets. This CPFE-based computational scheme, which is illustrated in Fig. 1, is based on the following steps:

(a) **Polycrystalline Representative Volume Element (RVE):** the RVE, also referred to as unit cell within the periodic homogenization scheme, is chosen to represent the polycrystalline medium. The unit cell is generated by the free software package NEPER [66] and the size of each individual grain is determined using the NEPER keyword '***statcell diameq***'. Furthermore, one of the key advantages of the numerical simulations is the ability to explore the influence of virtual grain size variations on mechanical behavior. When improved mechanical properties are observed for certain grain size distributions, these results may guide materials processing strategies, such as heat treatments, to produce microstructures with targeted grain sizes in practice.

(b) **Mesh generation:** the unit cells are meshed using the open-source software Gmsh [67], which discretizes the unit cell into several 8-node linear hexahedral elements with full integration (C3D8 elements in ABAQUS). Each integration point within these finite elements represents a single crystal, and a custom-developed Python script is used to assign the corresponding grain size to each integration point.

(c) **Initial crystallographic texture:** in this work, the initial texture is assumed to be randomly distributed and is virtually generated at the grain level using the ATEX software [68]. As experimental texture data for the specific material under study were not available, this virtual approach allows for a systematic investigation of the influence of crystallographic orientations and texture evolution. The orientation datasets obtained are subsequently used to plot the pole figures, which thus correspond to the initial texture of the entire polycrystalline aggregate. A Python script is developed to assign the same crystallographic orientation to all of the single crystals within the same grain. The aggregate consists of multiple grains, each discretized into finite elements. Each grain is assigned a unique initial crystallographic orientation, so that all Gauss points within the same grain share this identical initial orientation. In other words, although each Gauss point represents a single crystal, a grain may contain multiple Gauss points,

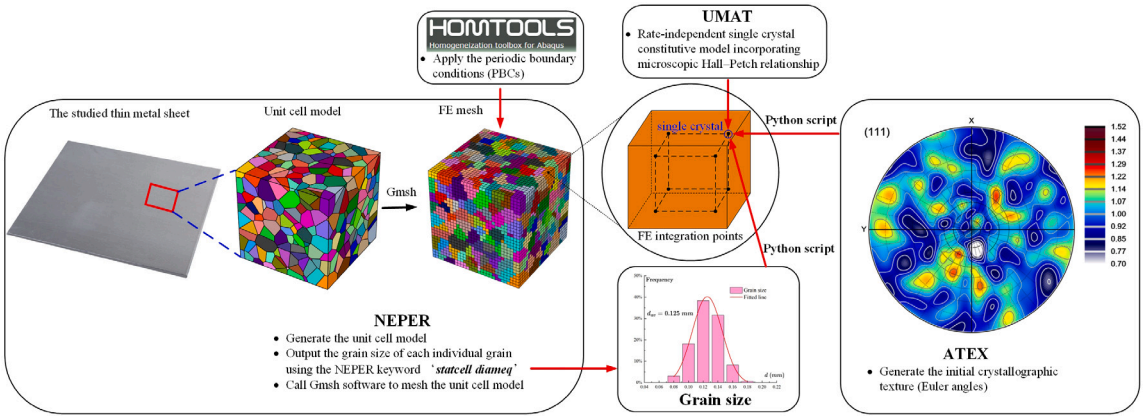

Fig. 1. Schematic of the developed Crystal Plasticity Finite Element Method (CPFEM) computational framework. The workflow consists in generating and meshing a Representative Volume Element (RVE) (NEPER, Gmsh), assigning an initial crystallographic texture (ATEX), and applying Periodic Boundary Conditions (PBCs) (HOMTOOLS) for simulations in ABAQUS/Standard. The custom-built UMAT incorporates a rate-independent crystal plasticity model with the microscopic Hall–Petch relationship to account for individual grain size effects.

effectively making it a collection of several single crystals with the same orientation. This full-field modeling approach, where individual grains and their orientations are explicitly defined, is distinct from mean-field or homogenized models (e.g., Taylor and VPSC schemes), which may assign a global texture to the material without resolving grain-level morphology explicitly. While that approach is common, the current study focuses on capturing local interactions and field heterogeneities. Experimentally, crystallographic orientations of grains are typically obtained through X-ray diffraction (XRD) or electron backscatter diffraction (EBSD). In the present modeling framework, grain boundaries are not explicitly modeled as separate interfaces with their own constitutive behavior (e.g., higher resistance or dislocation barriers). Instead, their effect is implicitly captured through the crystallographic orientation mismatch between neighboring grains. This mismatch induces deformation incompatibility, which forces localized plastic deformation and generates heterogeneity in the stress and strain fields, particularly near the grain boundaries. This approach, therefore, accounts for the primary mechanical role of grain boundaries in accommodating strain differences between adjacent crystals, an effect that is experimentally visualized through techniques like Kernel Average Misorientation (KAM) maps in EBSD analyses.

(d) **Microscopic constitutive equations:** the single crystal constitutive equations are formulated within a finite strain, rate-independent framework. These equations include the microscopic Hall–Petch relationship and a dislocation density-based hardening model to account for grain size effects. These constitutive equations are implemented in ABAQUS/Standard through a UMAT subroutine using a fully implicit integration scheme.

(e) **Periodic Boundary Conditions (PBCs):** the homogenization toolbox HOMTOOLS [69] is employed to automatically apply periodic boundary conditions (PBCs) and manage macroscopic loading.

The entire computational framework is carried out within ABAQUS/Standard. Finally, ductility limit strains are predicted using the Rice bifurcation theory, as further detailed in Section 2.5.

2.2. Periodic homogenization equations

The periodic homogenization technique, which links the macroscopic and microscopic scales, is adopted to determine the overall mechanical behavior of the unit cell from that of its single crystal constituents. To this end, the macroscopic deformation gradient $\mathbf{F}$ and the macroscopic first Piola–Kirchhoff stress tensor $\mathbf{P}$ are selected as appropriate work-conjugate deformation and stress measures. For the sake of brevity, only the key equations relevant to this technique are presented in this section:

- The macroscopic deformation gradient $\mathbf{F}$ and the macroscopic first Piola–Kirchhoff stress tensor $\mathbf{P}$ are linked to their microscopic counterparts $\mathbf{f}$ and $\mathbf{p}$ through the following volume averaging formulae:

$$\mathbf{F} = \frac{1}{|\mathcal{V}_0|}\int_{\mathcal{V}_0} \mathbf{f}\, d\mathcal{V}_0 \quad \text{and} \quad \mathbf{P} = \frac{1}{|\mathcal{V}_0|}\int_{\mathcal{V}_0} \mathbf{p}\, d\mathcal{V}_0, \tag{3}$$

where $\mathcal{V}_0$ is the initial volume of the unit cell. The rate form of these equations can be written as:

$$\dot{\mathbf{F}} = \frac{1}{|\mathcal{V}_0|}\int_{\mathcal{V}_0} \dot{\mathbf{f}}\, d\mathcal{V}_0 \quad \text{and} \quad \dot{\mathbf{P}} = \frac{1}{|\mathcal{V}_0|}\int_{\mathcal{V}_0} \dot{\mathbf{p}}\, d\mathcal{V}_0. \tag{4}$$

- The rate of the macroscopic deformation gradient $\dot{\mathbf{F}}$ is related to the macroscopic first Piola–Kirchhoff stress rate tensor $\dot{\mathbf{P}}$ through the macroscopic tangent modulus $\mathbb{B}$:

$$\dot{\mathbf{P}} = \mathbb{B} : \dot{\mathbf{F}}. \tag{5}$$

In this study, we focus on thin metal sheets subjected to biaxial loading. Thereby, the plane-stress assumption can be legitimately adopted. Under such an assumption, the macroscopic constitutive relation expressed in Eq. (5) can be reduced to its in-plane form:

$${}^{\mathrm{IN}}\dot{\mathbf{P}} = {}^{\mathrm{IN}}\mathbb{B} : {}^{\mathrm{IN}}\dot{\mathbf{F}}, \tag{6}$$

where tensors ${}^{\mathrm{IN}}\dot{\mathbf{P}}$, ${}^{\mathrm{IN}}\dot{\mathbf{F}}$, and ${}^{\mathrm{IN}}\mathbb{B}$ are defined by the following relations:

$${}^{\mathrm{IN}}\dot{\mathbf{P}} = \begin{bmatrix} \dot{P}_{11} & \dot{P}_{12} \\ \dot{P}_{21} & \dot{P}_{22} \end{bmatrix}; \quad {}^{\mathrm{IN}}\dot{\mathbf{F}} = \begin{bmatrix} \dot{F}_{11} & \dot{F}_{12} \\ \dot{F}_{21} & \dot{F}_{22} \end{bmatrix}; \quad \forall i,j,k,l = 1,2: \quad {}^{\mathrm{IN}}B_{ijkl} = B_{ijkl} - \frac{B_{ij33}B_{33kl}}{B_{3333}}. \tag{7}$$

- The microscopic static equilibrium equation, expressed in terms of the microscopic first Piola–Kirchhoff stress rate tensor $\dot{\mathbf{p}}$, is given by:

$$div_{\mathbf{x}_0}(\dot{\mathbf{p}}) = \mathbf{0}, \tag{8}$$

where $\mathbf{x}_0$ denotes the initial position of the material point.

- The kinematic localization relation assumes that the in-plane microscopic deformation gradient ${}^{\mathrm{IN}}\mathbf{f}$ can be additively decomposed into its macroscopic counterpart ${}^{\mathrm{IN}}\mathbf{F}$ and a superimposed periodic fluctuation gradient ${}^{\mathrm{IN}}\mathbf{f}_{per}$, as follows:

$$^{\mathrm{IN}}\mathbf{f} = {}^{\mathrm{IN}}\bar{\mathbf{F}} + {}^{\mathrm{IN}}\mathbf{f}_{per}. \tag{9}$$

The current in-plane coordinates $^{\mathrm{IN}}\mathbf{x}$ of a material point can be derived through spatial integration of Eq. (9), as follows:

$$^{\mathrm{IN}}\mathbf{x} = {}^{\mathrm{IN}}\bar{\mathbf{F}} \cdot {}^{\mathrm{IN}}\mathbf{x}_0 + {}^{\mathrm{IN}}\mathbf{u}_{per}, \tag{10}$$

where $^{\mathrm{IN}}\mathbf{u}_{per}$ is an in-plane periodic displacement fluctuation field. The in-plane velocity $^{\mathrm{IN}}\mathbf{v}$ of a material point can be further obtained by the time derivative of Eq. (10), as follows:

$$^{\mathrm{IN}}\mathbf{v} = {}^{\mathrm{IN}}\dot{\bar{\mathbf{F}}} \cdot {}^{\mathrm{IN}}\mathbf{x}_0 + {}^{\mathrm{IN}}\mathbf{v}_{per}, \tag{11}$$

where $^{\mathrm{IN}}\mathbf{v}_{per}$ is an in-plane periodic velocity fluctuation field.

- The constitutive equations at the single crystal scale are formulated in Section 2.3 below.

It should be noted that PBCs are applied at the level of the displacement and traction fields, not on the microstructural arrangement of grains. While the geometric distribution of grains in the RVE is not strictly periodic, the use of PBCs remains valid and appropriate for homogenization purposes, as it ensures continuity of deformation and traction across opposing faces of the unit cell (see, e.g., [70–75]). This approach, which pairs a realistic, non-periodic microstructure with periodic boundary conditions, has become the standard in computational materials science. The goal is to move beyond idealized, regular grain arrangements to use random, representative microstructures that capture the inherent variability of real materials, which is crucial for accurately predicting local mechanical phenomena [76]. The theoretical basis for this modeling approach lies in the statistical theory of RVEs for random media, which requires statistical, not geometrical, representativeness [77]. This principle has been successfully applied, not only in pioneering CPFEM studies of polycrystals [78], but is also a cornerstone of parallel numerical methods, such as the CP-FFT approach [79].

2.3. Size-dependent single crystal plasticity constitutive equations

In this work, the single crystal mechanical behavior is modeled within a finite strain rate-independent crystal plasticity framework. Within this framework, the microscopic elastoplastic deformation gradient $\mathbf{f}$ is multiplicatively decomposed into its elastic and plastic components $\mathbf{f}^e$ and $\mathbf{f}^p$, as follows:

$$\mathbf{f} = \mathbf{f}^e \cdot \mathbf{f}^p. \tag{12}$$

Furthermore, the elastic deformation gradient $\mathbf{f}^e$ can be expressed as the product of a stretching tensor $\mathbf{v}^e$ and a rotation tensor $\bar{\mathbf{r}}$, as follows:

$$\mathbf{f}^e = \mathbf{v}^e \cdot \bar{\mathbf{r}}, \tag{13}$$

where the rotation tensor $\bar{\mathbf{r}}$ defines the single crystal orientation with respect to the current configuration. This rotation matrix $\bar{\mathbf{r}}$ is typically expressed in terms of three Euler angles (φ_1, ϕ, φ_2), as follows:

$$\bar{\mathbf{r}} = \begin{bmatrix} cos\varphi_1 cos\varphi_2 - sin\varphi_1 sin\varphi_2 cos\phi & sin\varphi_1 cos\varphi_2 + cos\varphi_1 sin\varphi_2 cos\phi & sin\varphi_2 sin\phi \\ -cos\varphi_1 sin\varphi_2 - sin\varphi_1 cos\varphi_2 cos\phi & -sin\varphi_1 sin\varphi_2 + cos\varphi_1 cos\varphi_2 cos\phi & cos\varphi_2 sin\phi \\ sin\varphi_1 sin\phi & -cos\varphi_1 sin\phi & cos\phi \end{bmatrix}. \tag{14}$$

For efficient numerical treatment, the single crystal constitutive equations are formulated in an Eulerian framework. Within this framework, the microscopic velocity gradient $\mathbf{g}$ is obtained from the deformation gradient $\mathbf{f}$, as follows:

$$\begin{aligned} \mathbf{g} &= \dot{\mathbf{f}} \cdot \mathbf{f}^{-1} = \dot{\mathbf{f}}^e \cdot \mathbf{f}^{e-1} + \mathbf{f}^e \cdot \dot{\mathbf{f}}^p \cdot \mathbf{f}^{p-1} \cdot \mathbf{f}^{e-1}, \\ &= \dot{\mathbf{v}} \cdot \mathbf{v}^{e-1} + \mathbf{v}^e \cdot \dot{\bar{\mathbf{r}}} \cdot \bar{\mathbf{r}}^T \cdot \mathbf{v}^{e-1} + \mathbf{v}^e \cdot \bar{\mathbf{r}} \cdot \dot{\mathbf{f}}^p \cdot \mathbf{f}^{p-1} \cdot \bar{\mathbf{r}}^T \cdot \mathbf{v}^{e-1}. \end{aligned} \tag{15}$$

Since elastic deformation is generally much smaller than plastic deformation in most metallic materials, we assume that the stretching tensor $\mathbf{v}^e$ remains very close to the second-order identity tensor (i.e., $\mathbf{v}^e \approx \mathbf{I}_2$). Under this assumption, Eq. (15) simplifies to:

$$\mathbf{g} = \dot{\mathbf{v}}^e + \dot{\bar{\mathbf{r}}} \cdot \bar{\mathbf{r}}^T + \bar{\mathbf{r}} \cdot \dot{\mathbf{f}}^p \cdot \mathbf{f}^{p-1} \cdot \bar{\mathbf{r}}^T. \tag{16}$$

Additionally, this microscopic velocity gradient $\mathbf{g}$ can be additively decomposed into its symmetric part $\mathbf{d}$ (stretching rate) and antisymmetric part $\mathbf{w}$ (spin tensor), as follows:

$$\mathbf{g} = \mathbf{d} + \mathbf{w} = \frac{1}{2}(\mathbf{g} + \mathbf{g}^T) + \frac{1}{2}(\mathbf{g} - \mathbf{g}^T). \tag{17}$$

The stretching rate $\mathbf{d}$ and spin tensor $\mathbf{w}$ are further decomposed into their elastic and plastic components:

$$\begin{aligned} &\mathbf{d} = \mathbf{d}^e + \mathbf{d}^p; \quad \text{where} \quad \mathbf{d}^e = \dot{\mathbf{v}}^e \quad \text{and} \quad \mathbf{d}^p = \bar{\mathbf{r}} \cdot (\dot{\mathbf{f}}^p \cdot \mathbf{f}^{p-1})_{sym} \cdot \bar{\mathbf{r}}^T, \\ &\mathbf{w} = \mathbf{w}^e + \mathbf{w}^p; \quad \text{where} \quad \mathbf{w}^e = \dot{\bar{\mathbf{r}}} \cdot \bar{\mathbf{r}}^T \quad \text{and} \quad \mathbf{w}^p = \bar{\mathbf{r}} \cdot (\dot{\mathbf{f}}^p \cdot \mathbf{f}^{p-1})_{asym} \cdot \bar{\mathbf{r}}^T. \end{aligned} \tag{18}$$

Plastic deformation is assumed to solely occur through slip along crystallographic slip systems. Consequently, the plastic strain rate $\mathbf{d}^p$ and plastic spin rate $\mathbf{w}^p$ can be expressed as:

$$\mathbf{d}^p = \sum_{\alpha=1}^{N_s} \dot{\gamma}^\alpha \mathbf{R}^\alpha; \qquad \mathbf{w}^p = \sum_{\alpha=1}^{N_s} \dot{\gamma}^\alpha \mathbf{S}^\alpha, \tag{19}$$

where:

- N_s denotes the total number of crystallographic slip systems, with $N_s = 12$ for Face-Centered Cubic (FCC) materials, although the approach is applicable to other crystallographic structures.
- $\dot{\gamma}^\alpha$ denotes the slip rate on the α^{th} crystallographic slip system.
- $\mathbf{R}^\alpha$ and $\mathbf{S}^\alpha$ denote the symmetric and antisymmetric parts of the Schmid tensor $\vec{\mathbf{m}}^\alpha \otimes \vec{\mathbf{n}}^\alpha$ corresponding to the α^{th} slip system, which can be determined as follows:

$$\mathbf{R}^\alpha = \frac{1}{2}\left(\vec{\mathbf{m}}^\alpha \otimes \vec{\mathbf{n}}^\alpha + \vec{\mathbf{n}}^\alpha \otimes \vec{\mathbf{m}}^\alpha\right); \qquad \mathbf{S}^\alpha = \frac{1}{2}\left(\vec{\mathbf{m}}^\alpha \otimes \vec{\mathbf{n}}^\alpha - \vec{\mathbf{n}}^\alpha \otimes \vec{\mathbf{m}}^\alpha\right), \tag{20}$$

where $\vec{\mathbf{m}}^\alpha$ is the slip direction vector and $\vec{\mathbf{n}}^\alpha$ is the vector normal to the slip plane.

For computational efficiency, each slip system is decomposed into two oppositely oriented slip systems, denoted as $\left(\vec{\mathbf{m}}^\alpha, \vec{\mathbf{n}}^\alpha\right)$ for slip systems $\alpha = 1, \ldots, N_s$ and $\left(-\vec{\mathbf{m}}^{\alpha-N_s}, \vec{\mathbf{n}}^{\alpha-N_s}\right)$ for slip systems $\alpha = N_s + 1, \ldots, 2N_s$. This decomposition is adopted to manage only positive values of slip rates [80]. With this decomposition, Eq. (19) is transformed into:

$$\mathbf{d}^p = \sum_{\alpha=1}^{2N_s} \dot{\gamma}^\alpha \mathbf{R}^\alpha; \qquad \mathbf{w}^p = \sum_{\alpha=1}^{2N_s} \dot{\gamma}^\alpha \mathbf{S}^\alpha; \qquad \dot{\gamma}^\alpha \geq 0. \tag{21}$$

The rotation tensor $\bar{\mathbf{r}}$ is chosen such that the counterpart $\bar{\vec{\mathbf{m}}}^\alpha$ (resp. $\bar{\vec{\mathbf{n}}}^\alpha$) of $\vec{\mathbf{m}}^\alpha$ (resp. $\vec{\mathbf{n}}^\alpha$) in the intermediate configuration remains constant during deformation and equal to $\vec{\mathbf{m}}_0^\alpha$ (resp. $\vec{\mathbf{n}}_0^\alpha$). Vectors $\vec{\mathbf{m}}_0^\alpha$ and $\vec{\mathbf{n}}_0^\alpha$ are related to $\vec{\mathbf{m}}^\alpha$ and $\vec{\mathbf{n}}^\alpha$ by the following relations:

$$\vec{\mathbf{m}}^\alpha = \bar{\mathbf{r}} \cdot \vec{\mathbf{m}}_0^\alpha; \qquad \vec{\mathbf{n}}^\alpha = \vec{\mathbf{n}}_0^\alpha \cdot \bar{\mathbf{r}}^T, \tag{22}$$

where the components of vectors $\vec{\mathbf{m}}_0^\alpha$ and $\vec{\mathbf{n}}_0^\alpha$ for FCC single crystals, used in this study, are provided in Table 1.

To ensure objectivity of the single crystal constitutive equations, Eqs. (16), (18) and (21) can be expressed in the crystal lattice frame (intermediate configuration). To simplify the following presentation, tensors and vectors evaluated in this frame are marked with an overline notation ($\bar{\cdot}$). In this frame, the velocity gradient $\bar{\mathbf{g}}$ is given by:

$$\bar{\mathbf{g}} = \bar{\mathbf{r}}^T \cdot \mathbf{g} \cdot \bar{\mathbf{r}} = \bar{\mathbf{d}} + \bar{\mathbf{w}} = \bar{\mathbf{d}}^e + \bar{\mathbf{d}}^p + \bar{\mathbf{w}}^e + \bar{\mathbf{w}}^p, \tag{23}$$

where the plastic strain rate $\bar{\mathbf{d}}^p$ and the plastic spin rate $\bar{\mathbf{w}}^p$ can also be expressed in the crystal lattice frame as:

$$\bar{\mathbf{d}}^p = (\dot{\mathbf{f}}^p \cdot \mathbf{f}^{p-1})_{sym} = \sum_{\alpha=1}^{2N_s} \dot{\gamma}^\alpha \mathbf{R}_0^\alpha; \qquad \bar{\mathbf{w}}^p = (\dot{\mathbf{f}}^p \cdot \mathbf{f}^{p-1})_{asym} = \sum_{\alpha=1}^{2N_s} \dot{\gamma}^\alpha \mathbf{S}_0^\alpha; \qquad \dot{\gamma}^\alpha \geq 0. \tag{24}$$

Table 1
Crystallographic slip systems for FCC single crystals.

Slip system α	$\sqrt{3}\,\vec{\mathbf{n}}_0^\alpha$	$\sqrt{2}\,\vec{\mathbf{m}}_0^\alpha$
1	(111)	$[1\bar{1}0]$
2	(111)	$[10\bar{1}]$
3	(111)	$[01\bar{1}]$
4	$(\bar{1}11)$	[110]
5	$(\bar{1}11)$	[101]
6	$(\bar{1}11)$	$[01\bar{1}]$
7	$(1\bar{1}1)$	[110]
8	$(1\bar{1}1)$	$[10\bar{1}]$
9	$(1\bar{1}1)$	[011]
10	$(11\bar{1})$	$[1\bar{1}0]$
11	$(11\bar{1})$	[101]
12	$(11\bar{1})$	[011]

The elastic behavior is defined by the following hypoelastic law:

$$\dot{\bar{\boldsymbol{\sigma}}} = \bar{\mathbf{c}}^e : \bar{\mathbf{d}}^e = \bar{\mathbf{c}}^e : \bar{\mathbf{d}} - \sum_{\alpha=1}^{2N_s} \dot{\gamma}^\alpha \bar{\mathbf{c}}^e : \mathbf{R}_0^\alpha, \tag{25}$$

where $\bar{\mathbf{c}}^e$ represents the fourth-order elastic stiffness tensor. Elasticity is assumed to be isotropic, linear, and governed by the Hooke law.

The plastic flow of the single crystal is governed by the classical Schmid law, which states that crystallographic slip occurs only when the resolved shear stress τ^α reaches a critical threshold τ_c^α, as follows:

$$\forall \alpha = 1, \dots, 2N_s : \begin{cases} \tau^\alpha < \tau_c^\alpha & \Rightarrow \dot{\gamma}^\alpha = 0 \\ \tau^\alpha = \tau_c^\alpha & \Rightarrow \dot{\gamma}^\alpha \geq 0 \end{cases}, \tag{26}$$

where the resolved shear stress τ^α is defined as:

$$\forall \alpha = 1, \dots, 2N_s : \tau^\alpha = \bar{\boldsymbol{\sigma}} : \mathbf{R}_0^\alpha, \tag{27}$$

and its rate is expressed as:

$$\forall \alpha = 1, \dots, 2N_s : \dot{\tau}^\alpha = \dot{\bar{\boldsymbol{\sigma}}} : \mathbf{R}_0^\alpha. \tag{28}$$

The critical resolved shear stress τ_c^α is assumed to depend on the grain size and dislocation density, following the Hall–Petch relationship [27]:

$$\forall \alpha = 1, \dots, N_s : \tau_c^\alpha(\boldsymbol{\rho}, d^I) \hat{=} \tau_c^\alpha = \tau_c^{\alpha+N_s} = \tau_0 + \frac{\kappa_{HP}}{\sqrt{d^I}} + A\mu b \sqrt{h \sum_{\beta=1}^{N_s} \left(\rho^\beta + \rho^{\beta+N_s}\right)}, \tag{29}$$

where:

- A is a material constant,
- μ represents the shear modulus,
- b is the magnitude of the Burgers vector,
- ρ^β stands for the dislocation density on the β^{th} slip system,
- h is a hardening modulus. Here, hardening is assumed to be isotropic.
- d^I corresponds to the size of each individual grain, which is defined as the diameter of the sphere of equivalent volume. It can be obtained from experimental techniques, such as Electron Backscatter Diffraction (EBSD), or virtual microstructure generation method based on NEPER software. In the current formulation, the grain size d^I influences the hardening behavior through distinct and non-redundant physical mechanisms:
  - First, it impacts the initial yield stress. The term $\frac{\kappa_{HP}}{\sqrt{d^I}}$ is used to define the initial critical resolved shear stress (CRSS), as shown in Eq. (2). This term models the classical Hall–Petch effect.
  - Second, it affects the dynamic evolution of strain hardening. The grain size d^I also appears in the dislocation density evolution law (Eq. (30)), where it influences the rates of dislocation storage and annihilation. Physically, this reflects the role of grain boundaries as sites for dislocation absorption and their influence on the mean free path of dislocations, which governs the evolution of the dislocation density during plastic deformation.

  These two size effects operate at different stages and are therefore not redundant.

The evolution of the dislocation density $\dot{\rho}^\alpha$ is described by the Kocks law [29], as follows:

$$\forall \alpha = 1, \dots, N_s : \dot{\rho}^\alpha = \dot{\rho}^{\alpha+N_s} = \frac{1}{b}\left(\frac{1}{d^I} + \frac{\sqrt{\sum_{\beta=1,\beta\neq\alpha}^{N_s} \left(\rho^\beta + \rho^{\beta+N_s}\right)}}{K} - 2y_c\left(\rho^\alpha + \rho^{\alpha+N_s}\right)\right)\left(\dot{\gamma}^\alpha + \dot{\gamma}^{\alpha+N_s}\right), \tag{30}$$

where y_c is the critical annihilation length, associated with dynamic recovery, and K represents the dislocation storage coefficient. Considering Eq. (30), the evolution of the critical resolved shear stress $\dot{\tau}_c^\alpha$ can be expressed by differentiating Eq. (29), as follows:

$$\forall \alpha = 1, \dots, N_s : \dot{\tau}_c^\alpha = \dot{\tau}_c^{\alpha+N_s} \hat{=} \sum_{\beta=1}^{N_s} H^{\alpha\beta}\left(\dot{\gamma}^\beta + \dot{\gamma}^{\beta+N_s}\right),$$

$$\text{where} \quad H^{\alpha\beta} = \frac{A\mu\sqrt{h}}{2\sqrt{\sum_{k=1}^{N_s}\left(\rho^k + \rho^{k+N_s}\right)}} \times \left(\frac{1}{d^I} + \frac{\sqrt{\sum_{k=1,k\neq\beta}^{N_s}\left(\rho^k + \rho^{k+N_s}\right)}}{K} - 2y_c\left(\rho^\beta + \rho^{\beta+N_s}\right)\right). \tag{31}$$

The Schmid law defined by Eq. (26) can be reformulated as a non-linear complementarity problem (NLCP):

$$\forall \alpha = 1, \dots, 2N_s : \quad f^\alpha = \tau_c^\alpha - \tau^\alpha \geq 0; \quad \dot{\gamma}^\alpha \geq 0; \quad f^\alpha \dot{\gamma}^\alpha = 0. \tag{32}$$

Eq. (32) can be replaced by an equivalent mathematical system involving the semi-smooth Fischer–Burmeister function [81], as follows:

$$\forall \alpha = 1, \dots, 2N_s : \psi^\alpha = \sqrt{(f^\alpha)^2 + (\dot{\gamma}^\alpha)^2} - (f^\alpha + \dot{\gamma}^\alpha) = 0. \tag{33}$$

2.4. Numerical implementation

The constitutive equations at the single crystal scale are implemented into ABAQUS/Standard through a user-defined material subroutine (UMAT) programmed in FORTRAN. To efficiently solve the single crystal constitutive equations, a fully implicit numerical integration scheme based on the return-mapping algorithm [see64,82] is developed. This algorithm enables to incrementally integrate the single crystal constitutive equations presented in Section 2.3 over a typical time step $I^\Delta = [t_n, t_n + \Delta t]$, where Δt is the time increment given by the finite element (FE) solver. Unless explicitly stated otherwise, all variables expressed in the following developments are assumed to be evaluated at time $t_n + \Delta t$. At the beginning of each time step, the material parameters (elasticity constants, microscopic Hall–Petch and hardening parameters) as well as the mechanical variables $\bar{\mathbf{r}}$, $\boldsymbol{\sigma}$, γ^α, τ_c^α, ρ^α for $\alpha = 1, \dots, 2N_s$ are known at t_n. Another key input, the microscopic velocity gradient $\mathbf{g}$, which is assumed to remain constant over I^Δ, is approximated by the following equation:

$$\mathbf{g} = \left(\frac{\mathbf{f} - \mathbf{f}(t_n)}{\Delta t}\right) \cdot \left(\frac{\mathbf{f} + \mathbf{f}(t_n)}{2}\right)^{-1}. \tag{34}$$

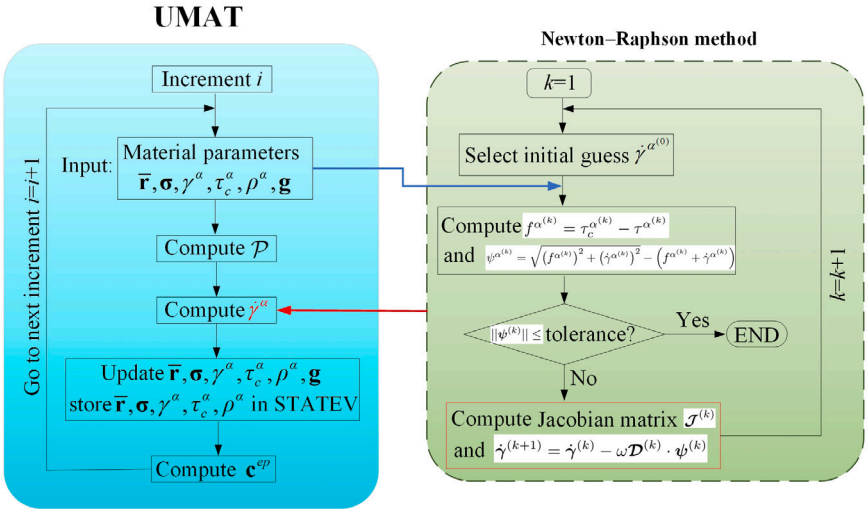

Fig. 2. Flowchart of the numerical integration scheme implemented in the UMAT subroutine. The left-hand side panel shows the main steps for each load increment, while the right-hand side panel details the iterative Newton–Raphson solver, based on the Fischer–Burmeister function, designed to determine the slip rates.

The main objective of this algorithm is to compute the unknown variables $\bar{\mathbf{r}}$, $\boldsymbol{\sigma}$, γ^α, τ_c^α, ρ^α for $\alpha = 1,\dots,2N_s$ and the microscopic consistent tangent modulus $\mathbf{c}^{ep}$ at time $t_n+\Delta t$. Fig. 2 shows the flow chart of the developed integration scheme.

The main steps of the developed implicit integration algorithm are outlined in the following subsections.

2.4.1. Determination of the set of potentially active slip systems

By analyzing the single crystal constitutive equations, it becomes clear that determining the set of active slip systems $\mathcal{A}$ and their corresponding slip rates $\dot{\gamma}^\alpha$ is sufficient to compute all of the unknown variables at $t_n+\Delta t$. To compute these slip rates, we first introduce the set of potentially active slip systems $\mathcal{P}$. In the return-mapping algorithm, a slip system is considered to be potentially active if its trial resolved shear stress τ^α_{trial} exceeds the corresponding critical resolved shear stress τ_c^α at t_n:

$$\mathcal{P}=\left\{\alpha=1,\dots,2N_s \,:\, \tau^\alpha_{trial}-\tau_c^\alpha(t_n)>0\right\}, \tag{35}$$

where the trial resolved shear stress τ^α_{trial} is calculated by projecting the trial stress $\bar{\boldsymbol{\sigma}}_{trial}$ onto tensor $\mathbf{R}_0^\alpha$:

$$\forall\alpha=1,\dots,2N_s \,:\, \tau^\alpha_{trial}=\bar{\boldsymbol{\sigma}}_{trial}:\mathbf{R}_0^\alpha. \tag{36}$$

In Eq. (36), the trial stress $\bar{\boldsymbol{\sigma}}_{trial}$ is determined by assuming that the mechanical behavior over the time increment is fully elastic:

$$\bar{\boldsymbol{\sigma}}_{trial}=\bar{\boldsymbol{\sigma}}(t_n)+\Delta t\,\dot{\bar{\boldsymbol{\sigma}}}=\bar{\boldsymbol{\sigma}}(t_n)+\Delta t\,\bar{\mathbf{c}}^e:\bar{\mathbf{d}}. \tag{37}$$

2.4.2. Determination of the slip rates for active slip systems

Once the set of potentially active slip systems $\mathcal{P}$ identified from Eq. (35), Eq. (33) can be reduced to the systems belonging to $\mathcal{P}$:

$$\forall\alpha\in\mathcal{P}\,:\,\psi^\alpha=\sqrt{(f^\alpha)^2+(\dot{\gamma}^\alpha)^2}-(f^\alpha+\dot{\gamma}^\alpha)=0. \tag{38}$$

In Eq. (38), the yield function f^α is defined by:

$$\forall\alpha\in\mathcal{P}\,:\,f^\alpha=\tau_c^\alpha-\tau^\alpha, \tag{39}$$

where the resolved shear stress τ^α and the critical resolved shear stress τ_c^α are computed using an implicit scheme, as follows:

$$\forall\alpha\in\mathcal{P}\,:\,\begin{cases}\tau^\alpha=\left(\bar{\boldsymbol{\sigma}}(t_n)+\Delta t\,\dot{\bar{\boldsymbol{\sigma}}}\right):\mathbf{R}_0^\alpha=\left(\bar{\boldsymbol{\sigma}}(t_n)+\Delta t\left(\bar{\mathbf{c}}^e:\bar{\mathbf{d}}-\sum\limits_{\beta\in\mathcal{P}}\dot{\gamma}^\beta\bar{\mathbf{c}}^e:\mathbf{R}_0^\beta\right)\right):\mathbf{R}_0^\alpha;\\ \tau_c^\alpha=\tau_c^\alpha(t_n)+\Delta t\,\dot{\tau}_c^\alpha=\tau_c^\alpha(t_n)+\Delta t\sum\limits_{\beta\in\mathcal{P}}H^{\alpha\beta}\dot{\gamma}^\beta.\end{cases} \tag{40}$$

The slip rates of the potentially active slip systems, and then the set of active slip systems $\mathcal{A}$, are determined by solving the set of Eqs. (38) using the Newton–Raphson method. In this method, the slip rate vector $\dot{\boldsymbol{\gamma}}$ is iteratively updated according to:

$$\dot{\boldsymbol{\gamma}}^{(k+1)}=\dot{\boldsymbol{\gamma}}^{(k)}-\omega\boldsymbol{\mathcal{D}}^{(k)}\cdot\boldsymbol{\psi}^{(k)}, \tag{41}$$

where superscript '(k)' corresponds to the Newton–Raphson iteration index k, and parameter ω is set to 0.5 to ensure numerical stability of the iterative scheme. The initial guess for the slip rate vector $\dot{\boldsymbol{\gamma}}^{(0)}$ is taken from the last converged slip rates of the previous time increment, which are stored in the state variable (SDV) of the UMAT. In Eq. (41), matrix $\boldsymbol{\mathcal{D}}$ is the inverse of the Jacobian matrix $\boldsymbol{\mathcal{J}}=\partial\boldsymbol{\psi}/\partial\dot{\boldsymbol{\gamma}}$, which is given by the following index form:

$$\forall\alpha,\beta\in\mathcal{P}\,:\,\mathcal{J}^{\alpha\beta}=\frac{\partial\psi^\alpha}{\partial\dot{\gamma}^\beta}=\frac{f^\alpha\frac{\partial f^\alpha}{\partial\dot{\gamma}^\beta}+\delta^{\alpha\beta}\dot{\gamma}^\alpha}{\sqrt{(f^\alpha)^2+(\dot{\gamma}^\alpha)^2}}-\frac{\partial f^\alpha}{\partial\dot{\gamma}^\beta}-\delta^{\alpha\beta}, \tag{42}$$

where $\partial f^\alpha/\partial\dot{\gamma}^\beta$ is given by the following expression:

$$\begin{aligned}\forall\alpha,\beta\in\mathcal{P}\,:\,\frac{\partial f^\alpha}{\partial\dot{\gamma}^\beta}&=\frac{\partial\tau_c^\alpha}{\partial\dot{\gamma}^\beta}-\frac{\partial\tau^\alpha}{\partial\dot{\gamma}^\beta};\\ &=\Delta t\left(H^{\alpha\beta}+\sum_{\zeta\in\mathcal{P}}\frac{\partial H^{\alpha\zeta}}{\partial\dot{\gamma}^\beta}\dot{\gamma}^\zeta+\mathbf{R}_0^\alpha:\bar{\mathbf{c}}^e:\mathbf{R}_0^\beta\right).\end{aligned} \tag{43}$$

Note that the Jacobian matrix $\boldsymbol{\mathcal{J}}$ may be singular. In such a case, the pseudo-inversion technique [83] is applied. The Newton–Raphson iterations are continued until the following convergence criterion is fulfilled:

$$\|\boldsymbol{\psi}^{(k)}\|\le 10^{-10}, \tag{44}$$

where $\|\bullet\|$ represents the *Euclidean* norm. After convergence, some slip systems belonging to set $\mathcal{P}$ may have slip rates $\dot{\gamma}^\alpha=0$ (inactive), while others will have strictly positive slip rates. The set of active slip systems

$\mathcal{A}$ is then determined by selecting the slip systems from $\mathcal{P}$ that satisfy $\dot{\gamma}^{\alpha} > 0$.

2.4.3. Variable update

Once the set of active slip systems $\mathcal{A}$ and their corresponding slip rates $\dot{\gamma}^{\alpha}$ determined, the unknown variables $\bar{\mathbf{r}}$, $\boldsymbol{\sigma}$, γ^{α}, τ_c^{α}, ρ^{α} at $t_n + \Delta t$ can be updated by the implicit scheme, as follows:

$$
\begin{cases}
\delta\bar{\mathbf{r}} = exp^{\left(\Delta t\left(\bar{\mathbf{w}} - \sum\limits_{\alpha\in\mathcal{A}} \dot{\gamma}^{\alpha}\mathbf{S}_0^{\alpha}\right)\right)}; \\
\bar{\mathbf{r}} = \bar{\mathbf{r}}(t_n)\cdot\delta\bar{\mathbf{r}}; \\
\dot{\bar{\boldsymbol{\sigma}}} = \bar{\mathbf{c}}^{e} : \left(\bar{\mathbf{d}} - \sum\limits_{\alpha\in\mathcal{A}} \dot{\gamma}^{\alpha}\mathbf{R}_0^{\alpha}\right); \\
\bar{\boldsymbol{\sigma}} = \bar{\boldsymbol{\sigma}}(t_n) + \Delta t\dot{\bar{\boldsymbol{\sigma}}}; \\
\boldsymbol{\sigma} = \bar{\mathbf{r}}\cdot\bar{\boldsymbol{\sigma}}\cdot\bar{\mathbf{r}}^{T}; \\
\forall\alpha = 1,\dots,2N_s : \gamma^{\alpha} = \gamma^{\alpha}(t_n) + \Delta t\dot{\gamma}^{\alpha}; \\
\forall\alpha = 1,\dots,N_s : \dot{\rho}^{\alpha} = \dot{\rho}^{\alpha+N_s} \\
\qquad = \frac{1}{b}\left(\frac{1}{d^{I}} + \frac{\sqrt{\sum\limits_{\beta=1,\beta\neq\alpha}^{N_s}\left(\rho^{\beta}(t_n) + \rho^{\beta+N_s}(t_n)\right)}}{K} - 2y_c\left(\rho^{\alpha}(t_n) + \rho^{\alpha+N_s}(t_n)\right)\right)\left(\dot{\gamma}^{\alpha} + \dot{\gamma}^{\alpha+N_s}\right); \\
\forall\alpha = 1,\dots,N_s : \rho^{\alpha} = \rho^{\alpha+N_s} = \rho^{\alpha}(t_n) + \Delta t\dot{\rho}^{\alpha}; \\
\forall\alpha = 1,\dots,N_s : \tau_c^{\alpha} = \tau_c^{\alpha+N_s} = \tau_c^{\alpha}(t_n) + \Delta t\sum\limits_{\beta\in\mathcal{A}} H^{\alpha\beta}\dot{\gamma}^{\beta}.
\end{cases}
\tag{45}
$$

Once the different variables updated by the previous fully implicit integration scheme, the microscopic consistent tangent modulus $\bar{\mathbf{c}}^{ep}$ needs to be derived. This derivation is crucial both for enhancing the convergence of the FE computations and also for conducting the bifurcation analysis. The consistent tangent modulus is given by the following expression (see more details in Zhou et al. [38,39]):

$$
\bar{\mathbf{c}}^{ep} = \frac{\partial\delta\bar{\boldsymbol{\sigma}}}{\partial\delta\bar{\boldsymbol{\varepsilon}}} = \bar{\mathbf{c}}^{e} - \sum_{\alpha\in\mathcal{A}}\sum_{\beta\in\mathcal{A}} Y^{\alpha\beta}(t_n)\left(\bar{\mathbf{c}}^{e} : \mathbf{R}_0^{\alpha} + \mathbf{S}_0^{\alpha}\cdot\bar{\boldsymbol{\sigma}}(t_n) - \bar{\boldsymbol{\sigma}}(t_n)\cdot\mathbf{S}_0^{\alpha}\right)\otimes\left(\mathbf{R}_0^{\beta} : \bar{\mathbf{c}}^{e}\right),
\tag{46}
$$

where matrix $\boldsymbol{Y}$ is the inverse of matrix $\wp$, with $\wp$ defined in the following index form:

$$
\forall\alpha,\beta\in\mathcal{A} : \wp^{\alpha\beta} = H^{\alpha\beta}(t_n) + \mathbf{R}_0^{\alpha} : \bar{\mathbf{c}}^{e} : \mathbf{R}_0^{\beta}.
\tag{47}
$$

The microscopic consistent tangent matrix $\mathbf{c}^{ep}$ in the current configuration can be easily obtained by adequately rotating its counterpart $\bar{\mathbf{c}}^{ep}$ using the rotation matrix $\bar{\mathbf{r}}$.

2.5. Rice bifurcation criterion

The ductility of a metal sheet, which refers to its ability to undergo significant deformation, is generally limited by the onset of localized necking. This phenomenon marks the critical deformation level that a metal sheet can withstand before potentially failing. A fundamental approach to predict the onset of localized necking has been proposed by the Rice bifurcation theory, established by Rice [84]. This theory is widely recognized in the literature as a robust and theoretically sound tool, unlike the initial imperfection approach developed by Marciniak and Kuczynski [85], which depends on the initial imperfection factor (which appears to be arbitrarily introduced and hardly physically justified). Macroscopic bifurcation is detected when the macroscopic constitutive equations loose ellipticity, resulting in a jump or discontinuity across a localization band. This localization band is defined by its normal vector, denoted as $\vec{\mathcal{N}}$, as illustrated in Fig. 3. The Rice bifurcation criterion is derived from the following three essential conditions:

- The kinematic compatibility condition, which results from the continuity of the velocity field across the band;
- The stress equilibrium condition between the zones inside and outside the band;
- The macroscopic constitutive relationships that govern the material behavior.

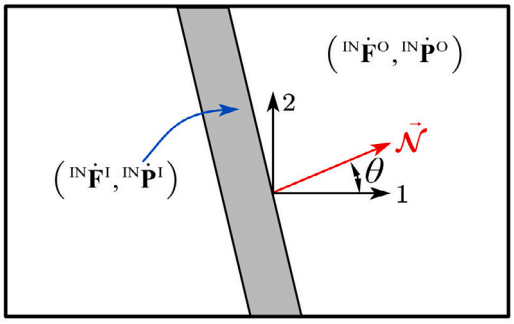

Fig. 3. Schematic of the Rice bifurcation criterion for predicting localized necking. A localization band (gray) with unit normal vector $\vec{\mathcal{N}}$ at an angle θ separates the material into regions inside (I) and outside (O) the band. Bifurcation occurs when the in-plane acoustic tensor becomes singular, indicating the onset of strain localization.

The main equations governing this criterion are summarized below:

Kinematic compatibility condition: this condition results from the continuity of the velocity field along the discontinuity surface, and can be formulated as follows:

$$
[[{}^{\mathrm{IN}}\dot{\mathbf{F}}]] = {}^{\mathrm{IN}}\dot{\mathbf{F}}^{\mathrm{O}} - {}^{\mathrm{IN}}\dot{\mathbf{F}}^{\mathrm{I}} = \dot{\vec{C}}\otimes\vec{\mathcal{N}},
\tag{48}
$$

where:

- $[[{}^{\mathrm{IN}}\dot{\mathbf{F}}]]$ represents the jump in the in-plane velocity gradient field ${}^{\mathrm{IN}}\dot{\mathbf{F}}$ across the localization band.
- ${}^{\mathrm{IN}}\dot{\mathbf{F}}^{\mathrm{O}}$ and ${}^{\mathrm{IN}}\dot{\mathbf{F}}^{\mathrm{I}}$ denote the in-plane velocity gradient outside and inside the localization band, respectively.
- $\dot{\vec{C}}$ is a jump vector.
- $\vec{\mathcal{N}}$ is the unit vector normal to the band, equals to $(cos\theta, sin\theta)$ for $0 \le \theta \le \pi/2$.

Stress equilibrium condition: the stress equilibrium condition can be expressed in terms of the macroscopic in-plane first Piola–Kirchhoff stress rate tensor ${}^{\mathrm{IN}}\dot{\mathbf{P}}$ across the localization band with normal vector $\vec{\mathcal{N}}$, as follows:

$$
[[{}^{\mathrm{IN}}\dot{\mathbf{P}}]]\cdot\vec{\mathcal{N}} = \vec{\mathbf{0}}.
\tag{49}
$$

Macroscopic constitutive relationship: defined by the generic Eq. (6).

By combining Eqs. (6), (48)–(49), the following expression is obtained:

$$
\vec{\mathcal{N}}\cdot\left[{}^{\mathrm{IN}}\mathbb{L} : \left(\dot{\vec{C}}\otimes\vec{\mathcal{N}}\right)\right] = \vec{\mathbf{0}},
\tag{50}
$$

where ${}^{\mathrm{IN}}\mathbb{L}$ is the transpose of the tangent modulus ${}^{\mathrm{IN}}\mathbb{B}$ by permutation of the first two indices:

$$
\forall i,j,k,l = 1,2 : {}^{\mathrm{IN}}L_{ijkl} = {}^{\mathrm{IN}}B_{jikl}.
\tag{51}
$$

Eq. (50) is equivalent to the following equation:

$$
\left(\vec{\mathcal{N}}\cdot{}^{\mathrm{IN}}\mathbb{L}\cdot\vec{\mathcal{N}}\right)\cdot\dot{\vec{C}} = \vec{\mathbf{0}},
\tag{52}
$$

where tensor $\vec{\mathcal{N}}\cdot{}^{\mathrm{IN}}\mathbb{L}\cdot\vec{\mathcal{N}}$ is the so-called in-plane acoustic tensor. Localized necking occurs when this tensor becomes singular, i.e., when its determinant vanishes:

$$
\det\left(\vec{\mathcal{N}}\cdot{}^{\mathrm{IN}}\mathbb{L}\cdot\vec{\mathcal{N}}\right) = 0.
\tag{53}
$$

Table 2
Material parameters corresponding to aluminum alloys, identified from data obtained under uniaxial tensile testing conditions.

	Notation	Value	Unit	Source
Elasticity	E	65	GPa	Yoshida and Kuroda [88]
	ν	0.3	–	Yoshida and Kuroda [88]
	μ	25	GPa	$\mu = E/2(1+\nu)$
Microscopic Hall–Petch constant	κ_{HP}	6.325	MPa $(\text{mm})^{1/2}$	Zhou et al. [39]
Dislocation density-based hardening	τ_0	50	MPa	Zhou et al. [38]
	h	1.0	–	This work
	b	2.86×10^{-7}	mm	Bratov and Borodin [89]
	A	0.4	–	Zhou et al. [38]
	ρ_0	1×10^{8}	mm^{-2}	Banerjee and Bhawalkar [90]
	y_c	$10\,b$	mm	Meng [91]
	K	10	–	Zhou et al. [38]

To apply the Rice bifurcation criterion, the macroscopic in-plane tangent modulus ${}^{\text{IN}}\mathbb{L}$ needs to be determined by the condensation technique [38,86,87]. Detailed procedures for this technique can be found in the works of Zhou et al. [38,39] and Zhu et al. [87]. Once ${}^{\text{IN}}\mathbb{L}$ computed, the localized necking criterion defined by Eq. (53) can be formulated as a minimization problem:

$$\text{Min}\left[\det\left(\vec{\mathcal{N}}\cdot{}^{\text{IN}}\mathbb{L}\cdot\vec{\mathcal{N}}\right)\right] \quad \text{for} \quad 0\le\theta\le\pi/2. \tag{54}$$

In Eq. (54), if the determinant value remains strictly positive over the different localization band orientations θ, then this indicates the absence of localized necking at the considered strain level. Conversely, the onset of localized necking is identified when $\text{Min}\left[\det\left(\vec{\mathcal{N}}\cdot{}^{\text{IN}}\mathbb{L}\cdot\vec{\mathcal{N}}\right)\right]$ reaches zero for the first time.

3. Results and discussions

In this section, the material parameters are first collected from various literature sources. Then, the effects of grain size on the strength and ductility limits of thin metal sheets both with uniform and gradient grain structures are extensively discussed. Finally, the strength and ductility limit trade-off is analyzed.

3.1. Identification of material parameters

In the present study, an aluminum alloy was selected as the representative material. The material parameters used in the different simulations are collected from previous contributions under uniaxial tensile testing conditions:

- Elasticity is assumed to be isotropic. This assumption is considered reasonable, as this study focuses on large strain phenomena, such as ductility limits, where the material response is dominantly influenced by plastic anisotropy, while the effects of elastic anisotropy are negligible. The isotropic elasticity parameters (E and ν) are referenced from Yoshida and Kuroda [88]. Then, the shear modulus μ, introduced in Eq. (29), is computed by the relation $\mu = E/2(1+\nu)$.
- The microscopic Hall–Petch constant κ_{HP} is given in Zhou et al. [39].
- The initial value of critical shear stress τ_0 and the parameters related to the evolution of dislocation density (A and K) are obtained from Zhou et al. [38].
- The other parameters related to the evolution of dislocation density, such as the magnitude of the Burgers vector b, the initial value of dislocation density ρ_0 and the critical annihilation length y_c are referenced from Bratov and Borodin [89], Banerjee and Bhawalkar [90] and Meng [91], respectively.
- The hardening modulus h is set to 1.0.

All of the material parameters used in the present work are listed in Table 2.

3.2. Unit cells with uniform grain structure

3.2.1. Presentation of the different unit cells and macroscopic loading

The main objective of this section is to assess the influence of the grain size and sheet thickness on the evolution of macroscopic strength. To achieve this, the average grain size d_{av} and the sheet thickness t are varied independently, as shown in Fig. 4. To investigate the effect of grain size, the unit cell volume is kept constant at 1.0 mm × 1.0 mm × 1.0 mm, while the average grain size d_{av} is reduced from 0.400 mm to 0.090 mm, as depicted in Fig. 4(a)–(e). The unit cells presented in Fig. 4(a)–(e) contain 27, 115, 383, 915 and 2370 grains, respectively. The corresponding histograms, displayed below each unit cell, illustrate the grain size distribution. The unit cells used to analyze the influence of the thickness t on the macroscopic strength are presented in Fig. 4(f)–(i), while maintaining a constant average grain size of 0.125 mm. The unit cells shown in Fig. 4(f)–(i) are composed of 175, 542, 915 and 1143 grains, respectively. All of the generated unit cells, which follow random texture to reflect realistic microstructural variability, are discretized into approximately 27000 finite elements and converted into ABAQUS input files ('.inp' file) using the Gmsh software. It is well established that increasing the number of finite elements (i.e., mesh refinement) enhances simulation accuracy. However, larger numbers of finite elements may lead to significantly higher computational costs. A sensitivity study is performed in Appendix A to validate the adequacy of the number of finite elements to be used in the simulations.

The unit cells are subjected to in-plane biaxial loading conditions (see Fig. 5), which are defined by the following generic forms in terms of prescribed components of macroscopic deformation gradient $\mathbf{F}$ and first Piola–Kirchhoff stress tensor $\mathbf{P}$:

$$\mathbf{F} = \begin{pmatrix} F_{11} & 0 & \bigstar \\ 0 & (F_{11})^{\rho} & \bigstar \\ \bigstar & \bigstar & \bigstar \end{pmatrix}; \qquad \mathbf{P} = \begin{pmatrix} \bigstar & \bigstar & 0 \\ \bigstar & \bigstar & 0 \\ 0 & 0 & 0 \end{pmatrix}, \tag{55}$$

where '★' represents unknown components that must be determined through finite element simulations, and ρ is the strain-path ratio. Unless explicitly stated otherwise, the strain-path ratio $\rho = -0.5$ (corresponding to a uniaxial tension state) is used throughout this study. To enforce biaxial loading and ensure a plane-stress state, periodic boundary conditions (PBCs) are applied to the opposite faces of the unit cell in the first and second directions, respectively, namely S_{01}^{-} and S_{01}^{+} as well as S_{02}^{-} and S_{02}^{+}. The surfaces in the third direction, S_{03}^{-} and S_{03}^{+}, are left unconstrained to satisfy plane-stress conditions. The macroscopic loading prescribed in Eq. (55) is implemented through three reference points (namely, $RP1$, $RP2$, and $RP3$). The constraint equations, which prescribe displacements or reaction forces at these reference points, are defined as follows:

$$\begin{cases} RP1: U_{11} = F_{11} - 1; \quad U_{12} = 0; \quad RF_{13} = 0, \\ RP2: U_{21} = 0; \quad U_{22} = (F_{11})^{\rho} - 1; \quad RF_{23} = 0, \\ RP3: RF_{31} = 0; \quad RF_{32} = 0; \quad RF_{33} = 0. \end{cases} \tag{56}$$

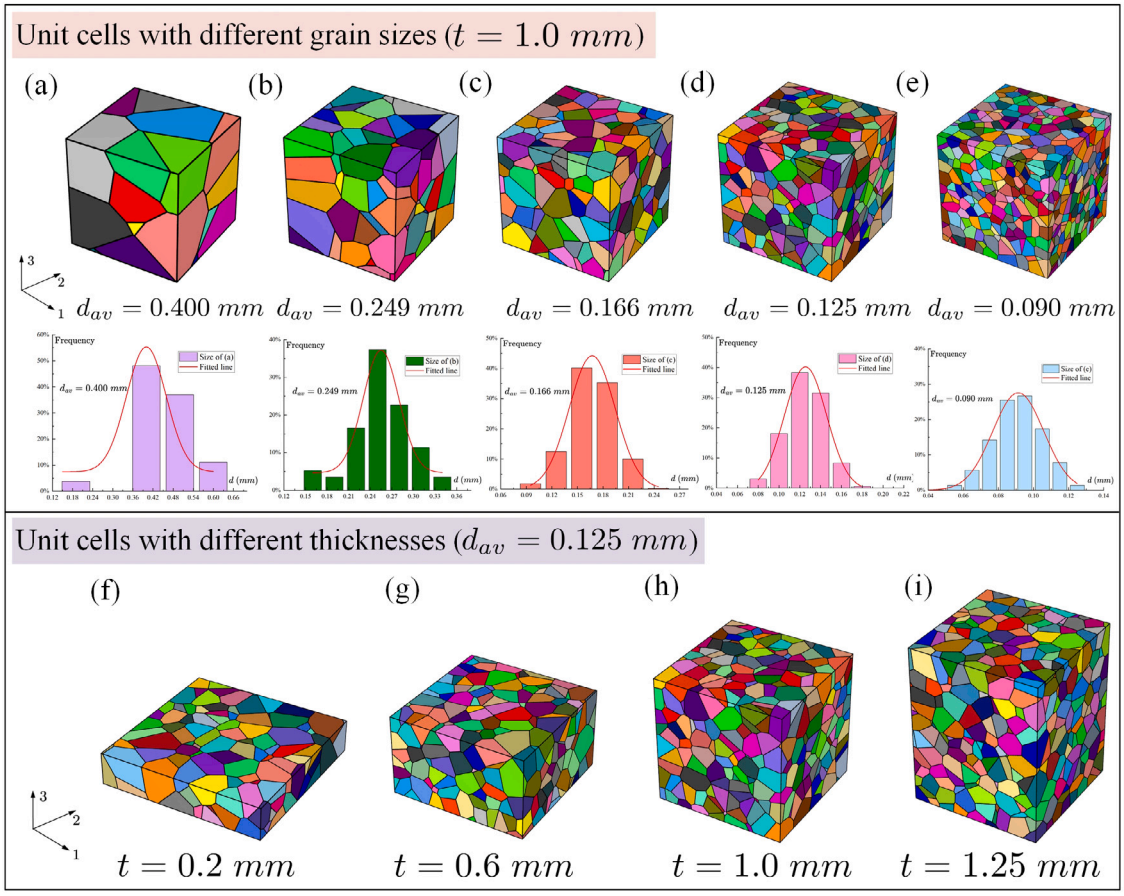

Fig. 4. Representative Volume Elements (RVEs) used to study size effects. (a)–(e) RVEs with constant thickness (t = 1.0 mm) and decreasing average grain size (d_{av}) used to investigate the Hall–Petch effect. Histograms show the corresponding grain size distributions. (f)–(i) RVEs with constant average grain size (d_{av} = 0.125 mm) and increasing thickness (t) used to study the effect of the thickness-to-grain size ratio (t/d_{av}).

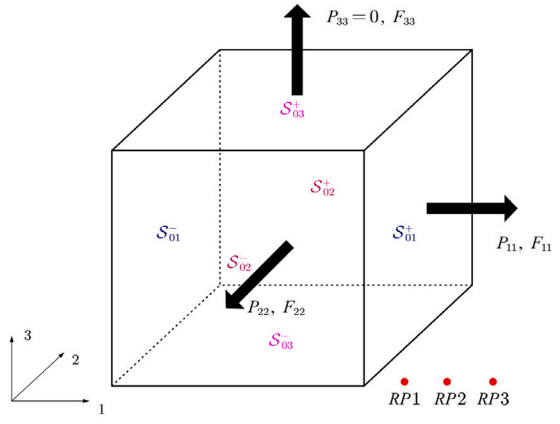

Fig. 5. Macroscopic boundary conditions for in-plane biaxial loading. Periodic Boundary Conditions (PBCs) are applied to the faces in the 1st and 2nd directions. The surfaces in the 3rd direction are left traction-free to enforce a plane-stress state. The macroscopic deformation is controlled via three reference points ($RP1$, $RP2$, $RP3$).

3.2.2. *Effect of grain size*

Fig. 6(a) displays the evolution of the macroscopic equivalent von Mises stress Σ_{eq} as a function of the macroscopic equivalent strain E_{eq} for different average grain sizes. As seen in Fig. 6(a), the macroscopic equivalent stress increases progressively with decreasing grain size, demonstrating the well-known strengthening phenomenon: 'the smaller, the stronger'. Fig. 6(b) illustrates the evolution of the strain hardening rate in terms of the macroscopic equivalent strain for the different grain sizes. It can be seen from Fig. 6(b) that the strain hardening curves reveal a declining trend, which is common to many materials. More importantly, the figure indicates that fine-grained materials exhibit superior work-hardening capabilities compared to coarse-grained materials. Fig. 6(c) shows the effect of grain size on the initial macroscopic equivalent yield stress. This result indicates that the grain refinement substantially enhances the initial macroscopic yield stress, thus underscoring the importance of reducing grain size for material strengthening. Fig. 6(d) depicts the Hall–Petch relationship between the predicted macroscopic equivalent yield stress $\Sigma_{eq,Yield}$ and the inverse square root of the average grain size, $1/\sqrt{d_{av}}$, at different levels of macroscopic equivalent strain E_{eq}: 0.2%, 2% and 5% (denoted by discrete points). The macroscopic Hall–Petch constant K_{HP} is obtained by applying a linear fit to the relationship between $\Sigma_{eq,Yield}$ and $1/\sqrt{d_{av}}$, represented by the solid lines in Fig. 6(d). It is evident from the results that the Hall–Petch constant increases with the macroscopic equivalent strain, rising from 19.992 MPa(mm)$^{1/2}$ at E_{eq} = 0.2% to 36.118 MPa(mm)$^{1/2}$ at E_{eq} = 5%. The increase of the macroscopic Hall–Petch constant K_{HP} with the macroscopic equivalent strain E_{eq} can be physically interpreted by the progressive accumulation and interaction of dislocations within the grains. At low strain levels, the dislocation density is relatively low, and the interaction between dislocations is limited. As plastic deformation progresses, dislocation storage and their interactions intensify, leading to increased internal resistance to plastic flow, thereby effectively enhancing the strain hardening of the material (see Eq. (31)). These numerical simulations not only effectively capture

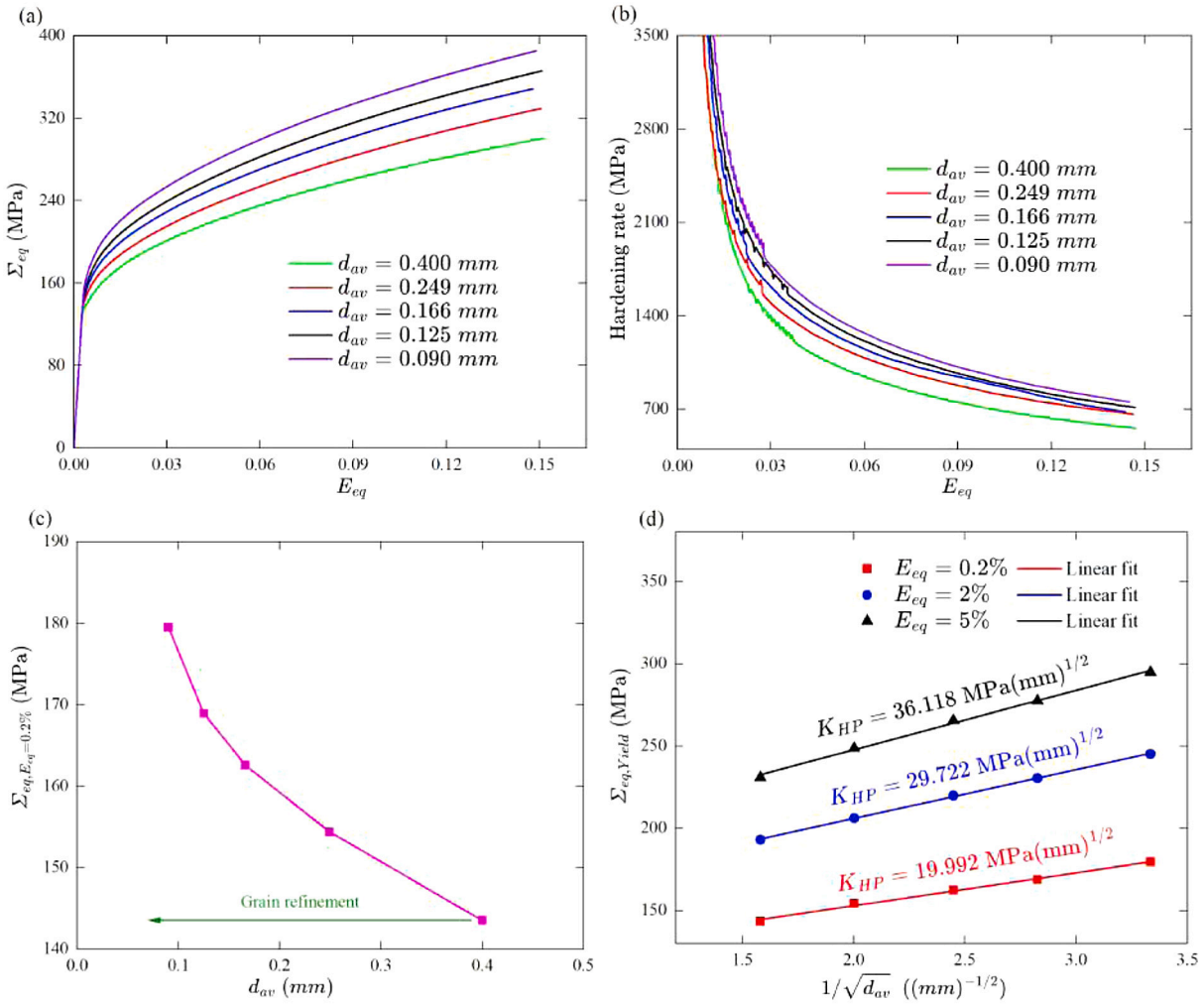

Fig. 6. Effect of grain size on: (a) macroscopic equivalent von Mises stress vs. macroscopic equivalent strain; (b) work-hardening behavior; (c) macroscopic equivalent yield stress at a strain level of $E_{eq} = 0.2\%$; (d) macroscopic equivalent yield stress vs. $1/\sqrt{d_{av}}$ at different strain levels (E_{eq} =0.2%, 2% and 5%). These curves clearly reflect the Hall–Petch effect, where macroscopic strength increases with decreasing grain size.

the grain size effect, but also demonstrate the predictive capabilities of the developed CPFE-based computational strategy.

3.2.3. *Effect of the initial dislocation density*

The initial dislocation density ρ_0 affects the critical resolved shear stress (CRSS) and hardening behavior (see Eqs. (29) and (31)). Furthermore, a higher initial dislocation density ρ_0 increases both dislocation generation and annihilation rates (see Eq. (30)), resulting in greater initial resistance to dislocation motion and earlier strain-hardening saturation. In this section, we investigate the effect of initial dislocation density ρ_0 on the macroscopic strength. For this purpose, we consider three different values of ρ_0: 1×10^8 mm^{-2}, 5×10^8 mm^{-2}, and 1×10^9 mm^{-2}. The predicted macroscopic equivalent von Mises stress–strain curves are presented in Fig. 7(a)–(c), which illustrate the significant dependence of the stress–strain responses on the grain size, whatever the selected value of initial dislocation density. These results demonstrate that the macroscopic equivalent stress consistently increases as the average grain size decreases. This behavior is observed for all of the levels of initial dislocation density ρ_0, highlighting the critical role of grain size in strengthening mechanisms. Moreover, we observe that the macroscopic strength decreases with increasing ρ_0. This phenomenon is attributed to faster dislocation annihilation relative to dislocation storage at higher dislocation densities, leading to a slower evolution of dislocation density and, consequently, influencing the rate of work hardening. These dynamics are detailed in Eqs. (30) and (31), which model the interplay between dislocation generation and annihilation processes. Support to our findings can be found in the work of Zhou et al. [38], who used a dislocation density-based mixed hardening model that did not account for the microscopic Hall–Petch relationship, yet similarly reported an influence of dislocation dynamics on macroscopic material properties. Further, Fig. 7(d) explores the relationship between macroscopic equivalent yield stress at a strain level of $E_{eq} = 0.2\%$ with error bars (relative to $\rho_0 = 1 \times 10^8$ mm^{-2}), and the inverse square root of the average grain size $1/\sqrt{d_{av}}$ for different initial dislocation densities. This result reveals that the initial dislocation density has a limited influence on the initial yield stress. The latter observation arises from the relatively small variation in the initial dislocation density.

3.2.4. *Effect of the loading strain path*

It is well known that the macroscopic behavior (strength, ductility, ...) is highly dependent on the applied loading. To better investigate this effect, the unit cells previously depicted in Fig. 4(a)–(e) are subjected to three specific biaxial strain paths: uniaxial tension ($\rho = -0.5$), plane-strain tension ($\rho = 0$), and equibiaxial tension ($\rho = 1$). The evolutions of the macroscopic equivalent von Mises stress as functions of macroscopic equivalent strain for these strain paths are illustrated in Fig. 8(a)–(c). These plots clearly show the influence of grain size

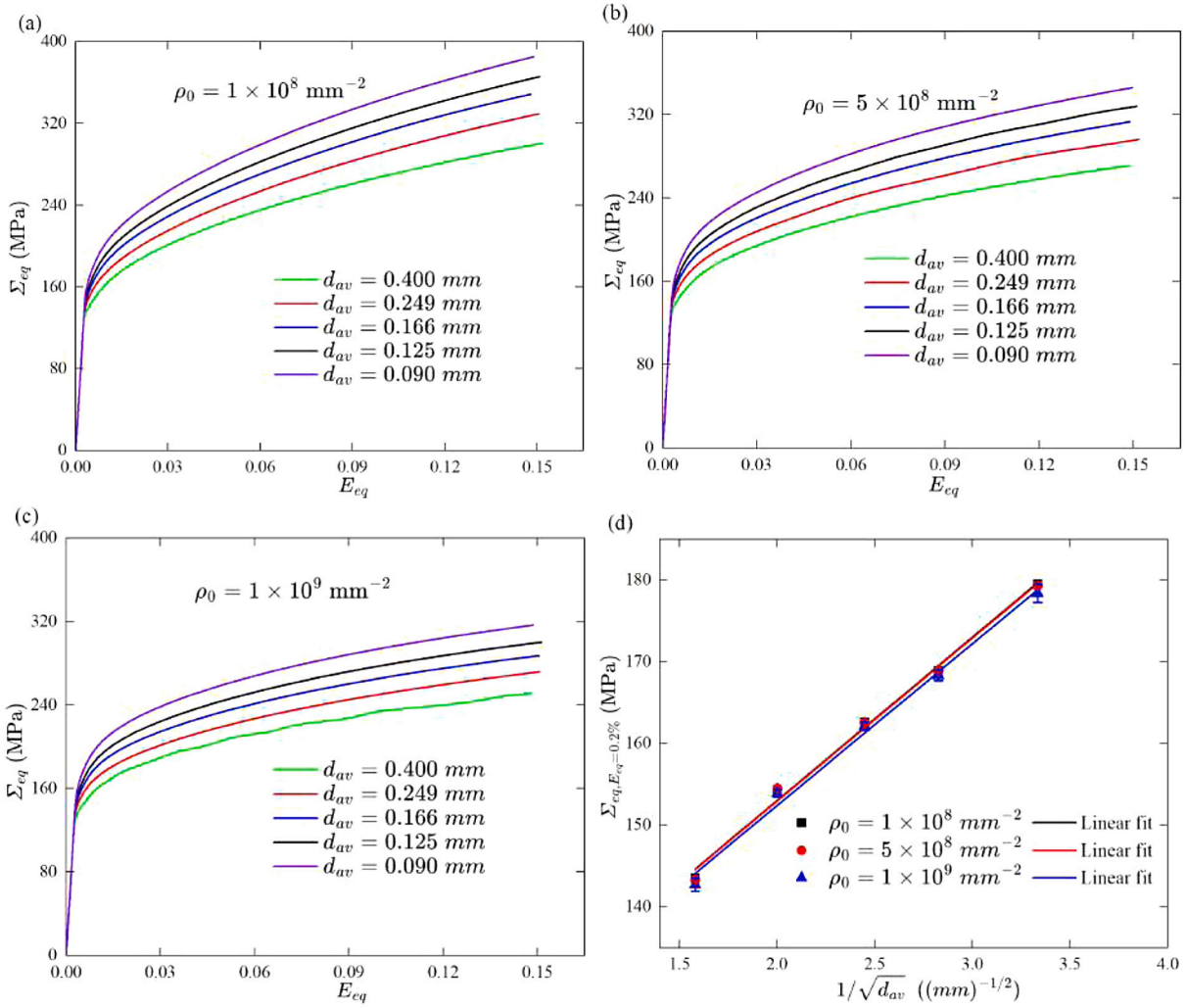

Fig. 7. Combined effect of grain size and initial dislocation density on macroscopic strength evolution for: (a) $\rho_0 = 1 \times 10^8$ mm^{-2}; (b) $\rho_0 = 5 \times 10^8$ mm^{-2}; (c) $\rho_0 = 1 \times 10^9$ mm^{-2}; (d) initial macroscopic equivalent yield stress at $E_{eq} = 0.2\%$ vs. $1/\sqrt{d_{av}}$. These results demonstrate that the predicted macroscopic equivalent stress consistently increases as the average grain size decreases.

on macroscopic strength under various loading conditions. Notably, the trend of increasing strength with decreasing grain size is observed consistently for all of the loading paths. This result reaffirms the significant role of microstructural characteristics, such as grain size, in determining the material response under different loading conditions. Furthermore, Fig. 8(d) provides the macroscopic equivalent yield stress at macroscopic equivalent strain $E_{eq} = 0.2\%$ against the inverse square root of average grain size $1/\sqrt{d_{av}}$ for each loading path, supplemented with error bars (relative to uniaxial tension) to indicate variability. Based on these results, it can be concluded that the initial macroscopic yield stress exhibits substantial sensitivity to the loading conditions in both coarse and fine-grained scenarios, while minimal sensitivity for intermediate-grain sizes.

3.2.5. *Effect of the unit cell thickness*

Fig. 9(a) presents the impact of unit cell thickness on the macroscopic equivalent von Mises stress Σ_{eq} as a function of the macroscopic equivalent strain E_{eq}. It is evident that the thickness of the unit cell plays a crucial role in dictating the mechanical response of the material. Specifically, an increase in unit cell thickness correlates with a marked enhancement in macroscopic mechanical strength. Notably, thicker unit cells exhibit superior mechanical strength when the average grain size remains constant. This enhancement in macroscopic strength with unit cell thickness can be attributed to the reduced relative impact of surface effects and constraints on dislocation movement within thicker samples. As thickness increases, the volume fraction of material influenced by surface-related phenomena decreases, allowing more uniform dislocation activity and strain distribution throughout the bulk of the material. Moreover, this study reveals that the rate of enhancement in macroscopic strength decreases as the thickness increases, indicating a saturation effect of the unit cell thickness and macroscopic strength. This behavior aligns closely with the experimental findings of Hug and Keller [92], who demonstrated similar patterns in the variation of flow stress relative to the thickness-to-grain size ratio t/d for polycrystalline nickel. Fig. 9(b) shows the macroscopic equivalent yield stress at $E_{eq} = 0.2\%$ as a function of the unit cell thickness-to-average grain size ratio (t/d_{av}). The results reveal a consistent trend of increasing the initial macroscopic yield stress with t/d_{av}. This trend reaffirms the influence of the unit cell thickness on material strength and aligns with the findings of Mahabunphachai and Koç [93], further supported by extensive literature.

3.3. *Unit cells with gradient grain structure*

A typical gradient structure material can be fabricated by surface modifications or treatments. The orientation of the gradient can lead to various arrangements of grain sizes. In this section, we explore

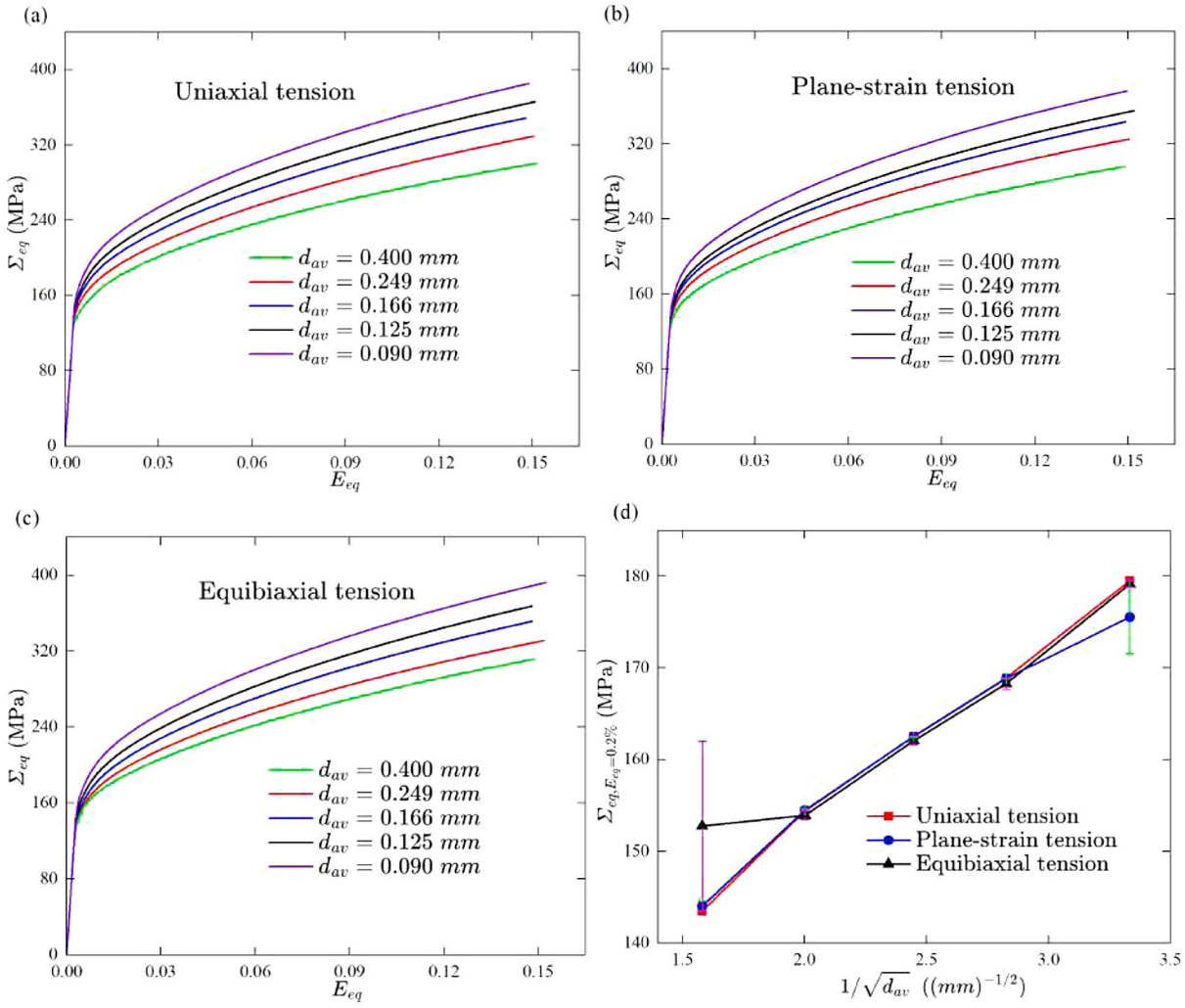

Fig. 8. Combined effect of grain size and strain path on macroscopic strength evolution for: (a) uniaxial tension ($\rho = -0.5$); (b) plane-strain tension ($\rho = 0$); (c) equibiaxial tension ($\rho = 1$); (d) macroscopic equivalent yield stress at $E_{eq} = 0.2\%$ vs. $1/\sqrt{d_{av}}$. These results indicate that the initial macroscopic yield stress exhibits substantial sensitivity to the loading conditions.

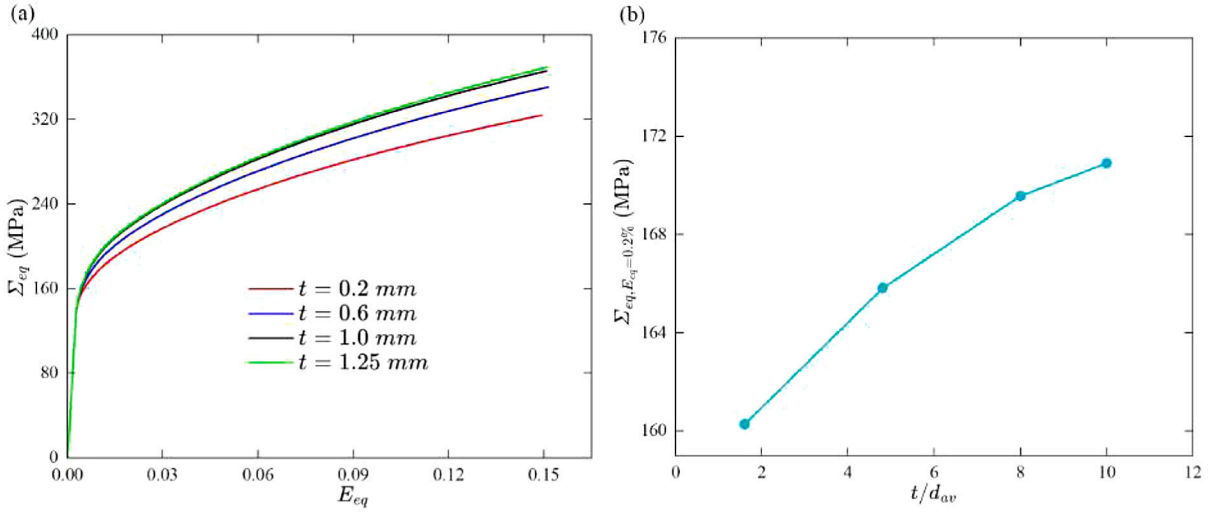

Fig. 9. Effect of sheet thickness (t) or thickness-to-average grain size ratio (t/d_{av}) for a constant average grain size ($d_{av} = 0.125\,\text{mm}$). (a) Stress–strain curves show that strength increases with sheet thickness. (b) The initial yield stress is plotted as a function of the thickness-to-average grain size ratio (t/d_{av}), thus confirming this strengthening trend.

the influence of gradient grain structures within unit cells, specifically focusing on the effect of grain size arrangements on mechanical properties. In this study, three distinct structures are introduced as follows:

- **Structure I (FC)**: characterized by a positive gradient, this structure transitions from fine to coarse grains. Such a gradient is expected to exhibit varying mechanical responses across its dimension, potentially affecting properties like strength and ductility deferentially across the unit cell.
- **Structure II (CFC)**: this configuration features a central fine grain layer flanked by coarse grains. This arrangement may lead to interesting stress distribution patterns under load, especially near the transitions between fine and coarse grains, influencing crack propagation paths and stress concentration points.
- **Structure III (FCF)**: incorporates a fine-coarse-fine grain sequence. This setup is particularly relevant for studying interfaces between different grain sizes and their role in mechanical performance, including the impact on yield strength and fracture toughness.

Fig. 10(a)–(c) visualizes these unit cells generated by the NEPER software. The generation process involves externally importing seeds via a Python script designed to produce a gradient distribution of grain sizes. Notably, while these unit cells display diverse grain size distributions, they maintain a consistent average grain size and a total grain number analogous to that depicted in Fig. 4(d). The minimum and maximum grain sizes of these unit cells are also provided in Fig. 10(a)–(c). The unit cells are discretized into approximately 27000 finite elements, consistent with the methodology outlined in Section 3.2, using the Gmsh software. The mesh sensitivity study is also conducted in Appendix A. The simulations employ the same initial crystallographic texture and loading boundary conditions as those used in Fig. 4(d) and described in Section 3.2, respectively. This approach enables comprehensive investigation of the impact of gradient effects on mechanical properties. Furthermore, it provides insights for the development and optimization of materials with tailored grain structures to meet specific engineering application requirements.

Fig. 10(d) displays the macroscopic equivalent von Mises stress Σ_{eq} as a function of the macroscopic equivalent strain E_{eq} for the different gradient grain structures. A key observation from this figure is the nearly identical initial yield stress for all of the unit cells, despite differences in their grain size gradients. In the first stages of loading, the stress–strain curves for the FC (fine to coarse), CFC (coarse to fine to coarse), and FCF (fine to coarse to fine) structures coincide closely, indicating a uniform response at the onset of plastic deformation. This result suggests that the initial macroscopic mechanical response is insensitive to the spatial distribution of grain sizes within the unit cell. However, as plastic strain increases, slight differences appear among the curves, indicating slight variations in strength that correlate with the arrangement of grain sizes. Interestingly, a slight increase in macroscopic strength is observed with increasing average grain size. This observation appears to contradict the conventional Hall–Petch relationship, which states that smaller grains typically enhance strength by providing more obstacles to dislocation motion. This deviation can be attributed to the unique effects of gradient grain structures. The presence of a gradient in grain sizes may introduce local stress and strain gradients and influence dislocation accumulation in ways that differ from homogeneously structured materials. These findings are also consistent with other numerical investigations reported in the literature, such as those by Lyu et al. [94], who observed that the fine-grained regions consistently showed lower strain levels compared to the coarse-grained zones. As the macroscopic deformation increases, the strain and stress gradients become more pronounced, reflecting the different deformation capabilities of fine and coarse grains due to their contrasting slip activity and hardening behavior. Additionally, this behavior emphasizes the complexity of material responses when featuring non-uniform internal structures, and highlights the need for further investigation to deepen our understanding of how gradient configurations impact material properties beyond conventional theories.

3.4. Effect of grain size distribution on the macroscopic behavior

3.4.1. Macroscopic strength

In this section, we analyze the influence of grain size distribution (both uniform and gradient structures) on the evolution of macroscopic strength. Based on the results of Fig. 10(d), which indicate a slight dependency of strength on gradient grain structures, Structure I (FC) is selected as the representative gradient grain structure model for this comparative study. For uniform grain structures, two unit cells from Fig. 4 are chosen for comparison: one with the average grain size d_{av} of 0.090 mm, denoted as UF (d_{av} = 0.090 mm), and the other with d_{av} of 0.400 mm, denoted as UF (d_{av} = 0.400 mm). Notably, the d_{av} of UF (d_{av} = 0.090 mm) corresponds to twice the minimum grain size d_{min}, and the d_{av} of UF (d_{av} = 0.400 mm) is approximately equal to the maximum grain size d_{max} of the gradient grain Structure I. As shown in Fig. 11, the initial yield stress of the gradient grain structure unit cell is approximately 161.17 MPa, which is about 13% higher than that of the UF (d_{av} = 0.400 mm). This result indicates a significant enhancement in macroscopic strength due to the gradient grain structure compared to the uniform grain structure with a larger average grain size, yet it remains lower than that of the UF (d_{av} = 0.090 mm). These findings are supported by the studies conducted by Wang et al. [95] and Liu et al. [62]. In Wang et al. [95], they investigated the grain size effect by incorporating the macroscopic Hall–Petch relationship into the Gurson–Tvergaard–Needleman (GTN) model, and both uniform and gradient grain structure models were subjected to uniaxial tension. In the study of Liu et al. [62], the strain gradient crystal plasticity (SGCP) theory has been employed to numerically examine the strength and ductility of gradient-structured CoCrFeMnNi high-entropy alloys under shear loading. In their predictions, the size effect has been attributed to the increased density of geometrically necessary dislocations (GNDs), which are critical in strengthening mechanisms. In addition, this analysis demonstrates the importance of considering grain size distributions in the material design process, due to their significant influence on the mechanical properties.

3.4.2. Macroscopic ductility limit

In this section, a comparative study is conducted to analyze the effect of grain size distribution on the ductility limits predicted by the Rice bifurcation criterion. The unit cells described in Section 3.4.1 serve as the basis for this comparative study. As highlighted in Section 2.5, the in-plane macroscopic tangent modulus ${}^{\mathrm{IN}}\mathbb{L}$ plays a pivotal role in the determination of the ductility limit. To emphasize its significance, the evolutions of its components ${}^{\mathrm{IN}}L_{1111}$ and ${}^{\mathrm{IN}}L_{1212}$, as functions of the macroscopic major strain E_{11} ($= Ln(F_{11})$), are plotted for different grain size distributions in Fig. 12(a)–(b). The results show that ${}^{\mathrm{IN}}L_{1111}$ decreases monotonically with increasing macroscopic major strain. On the other hand, the shearing component ${}^{\mathrm{IN}}L_{1212}$ experiences a significant reduction and stabilizes at a relatively low magnitude (approximately 3000 MPa), compared to its elastic magnitude of 25000 MPa. This feature is a consequence of the multi-slip nature of rate-independent crystal plasticity governed by the classical Schmid law. The pronounced reduction of this shearing component is the main destabilizing factor that promotes bifurcation. It is noteworthy that the shearing component remains nearly at its elastic level for rate-dependent models and rate-independent models with a regularized version of the Schmid law [82,96–98]. As a result, bifurcation is not observed at realistic strain levels in such constitutive models.

The evolution of the cubic root of the minimum of the determinant of the in-plane macroscopic acoustic tensor, denoted as

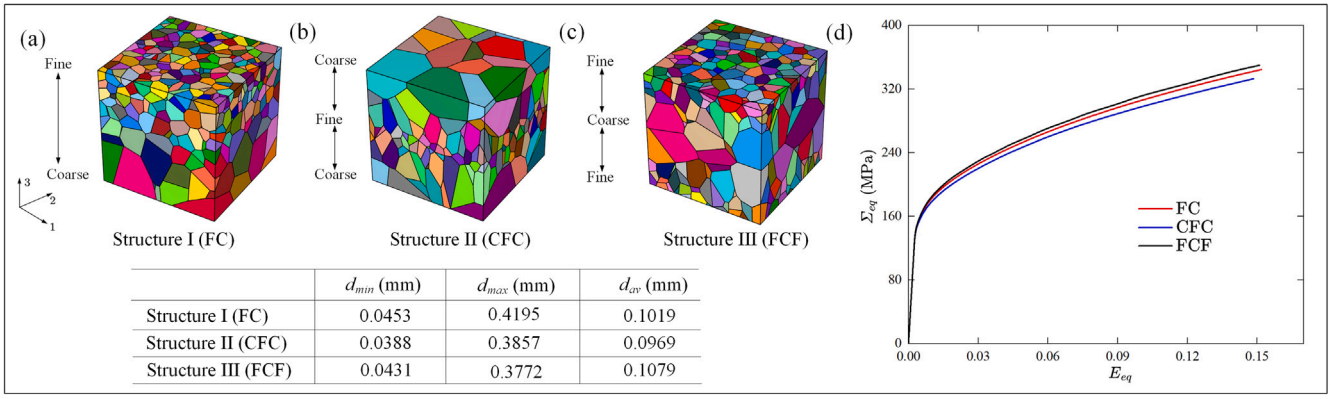

	d_{min} (mm)	d_{max} (mm)	d_{av} (mm)
Structure I (FC)	0.0453	0.4195	0.1019
Structure II (CFC)	0.0388	0.3857	0.0969
Structure III (FCF)	0.0431	0.3772	0.1079

Fig. 10. Gradient grain structures and their effect on macroscopic mechanical strength. (a) Fine-to-Coarse (FC), (b) Coarse-Fine-Coarse (CFC), and (c) Fine-Coarse-Fine (FCF) structures. All RVEs have similar average grain sizes. (d) The corresponding stress–strain curves show nearly identical initial yield stresses, with only minor deviations in hardening behavior at larger strains.

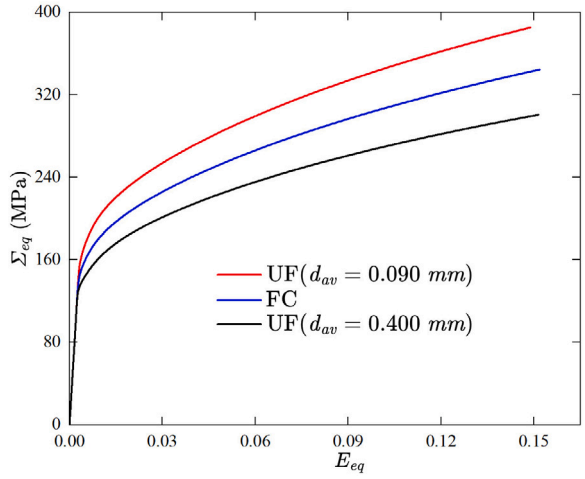

Fig. 11. Comparison of macroscopic strength for uniform and gradient grain structures. The gradient (FC) structure shows significantly higher strength than the uniform coarse-grained (UF, $d_{av} = 0.400$ mm) structure, but lower than the uniform fine-grained (UF, $d_{av} = 0.090$ mm) one.

Min $\left[\det\left(\vec{\mathcal{N}} \cdot {}^{\mathrm{IN}}\mathbb{L} \cdot \vec{\mathcal{N}}\right)\right]^{1/3}$, is plotted as a function of the macroscopic major strain E_{11} in Fig. 12(c). According to the Rice bifurcation theory outlined in Section 2.5, bifurcation and thus the onset of localized necking occurs when this determinant reaches zero, which is indicated by the green points on the curves in Fig. 12(c). These plots reveal that the ductility limit is distinctly influenced by the grain size distribution:

- The gradient grain structure model (FC) provides a higher ductility limit compared to the uniform grain structure with a smaller, yet very close, average grain size (UF (d_{av} = 0.090 mm)). The improved ductility limit observed in gradient structures primarily arises from the redistribution of strain due to the grain size gradient, as demonstrated by Wang et al. [95]. This result suggests that the arrangement of grains from fine to coarse within the unit cell may contribute to a more gradual and distributed strain localization, delaying the onset of plastic strain localization.
- The ductility limit of the gradient grain structure model (FC) is still lower than that of the uniform coarse grain structure (UF (d_{av} = 0.400 mm)), which indicates that larger grains consistently enhance ductility more significantly than graded microstructures. This effect is due to the dislocation movement over longer distances within each grain before encountering obstacles (such as grain boundaries) in coarse-grained materials, which can delay the propagation of localized deformation, thus enhancing the overall ductility.

This approach helps in understanding the ductility limits of materials under extreme deformation conditions. Specifically, the results confirm the potential of gradient grain structures to enhance ductility in materials where large grains are inevitable or desirable for other reasons, such as thermal stability or corrosion resistance. Such insights can guide the development of advanced materials for critical applications in aerospace, automotive, etc.

3.4.3. *Strength and ductility trade-off*

Fig. 13 presents the relationship between the initial macroscopic yield strength and the macroscopic major strain E_{11} at the onset of strain localization for uniform and gradient grain structures. Traditionally, grain refinement leads to an increase in the initial yield stress, whereas a decrease in ductility, as illustrated by the black points in Fig. 13. This trade-off results in a concave-like curve depicting these two properties, thus reflecting the inherent limitations of uniform grain structures. It is important to note, however, that the results reveal a unique pattern when gradient grain structures are employed. Specifically:

- **Coarse Grain Structure:** exhibits higher ductility but lower yield strength, which is typical for materials with larger grains. Larger grains can accommodate more plastic deformation before reaching strain localization, but they generally exhibit lower yield strength due to fewer obstacles to dislocation movement.
- **Fine Grain Structure:** provides enhanced yield strength due to the Hall–Petch effect, where smaller grains hinder the movement of dislocations more effectively. However, this fine-grained material exhibits lower ductility, owing to the lack of strain hardening capacity.
- **Gradient Grain Structure:** represents a combination of coarse and fine grain structures, resulting in improved strength–ductility trade-off. Such gradient grain structure is positioned above the traditional uniform grain refinement region, as indicated by the red star in Fig. 13. While enhancements in strength and ductility seem to be limited, further improvements can be achieved by optimizing the layering and spatial arrangement of gradient-grained structures, particularly at lower temperatures [99].

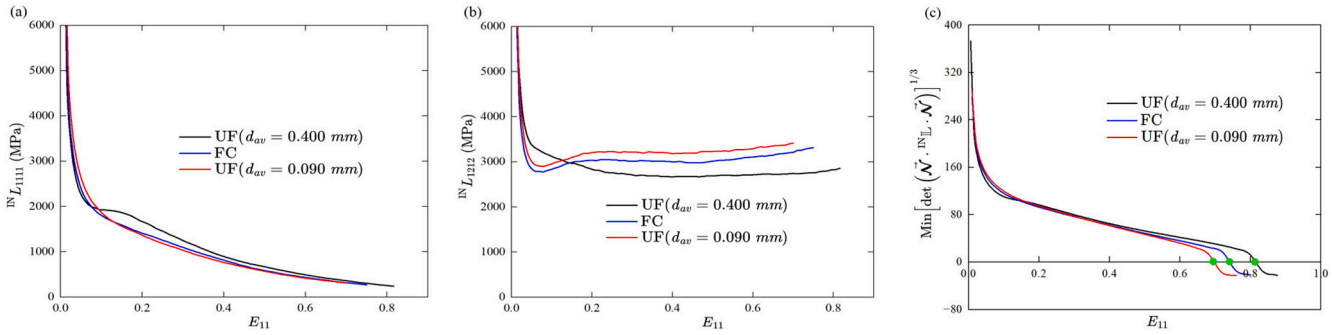

Fig. 12. Bifurcation analysis for ductility limit prediction. (a)–(b) Evolution of the key components of the in-plane macroscopic tangent modulus ${}^{\mathrm{IN}}L_{1111}$ and ${}^{\mathrm{IN}}L_{1212}$. (c) Evolution of the cubic root of the minimum of the determinant of the acoustic tensor $\vec{\mathcal{N}} \cdot {}^{\mathrm{IN}}\mathbb{L} \cdot \vec{\mathcal{N}}$. The onset of localized necking is predicted when this determinant reaches zero (green dots). The results show that the coarse-grained structure results in the highest ductility, while the gradient structure offers clear ductility improvement over the fine-grained one.

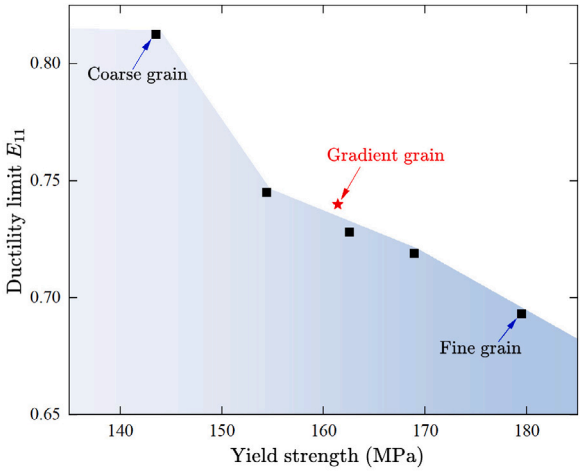

Fig. 13. Strength and ductility trade-off, characterized by the initial macroscopic yield strength and the macroscopic major limit strain E_{11}. The gradient grain structure (red star) is positioned above this traditional trade-off curve, demonstrating its ability to simultaneously enhance both strength and ductility.

The gradient grain structure, therefore, stands out as one of the strategic approaches in material design, offering improvements in both yield strength and ductility. This is achieved by tailoring the spatial distribution of grain sizes to harness the mechanical advantages of both fine and coarse grains effectively. Such a strategy is particularly valuable in applications requiring enhanced strength and ductility, such as automotive or aerospace components. This investigation reveals the critical importance of grain structure control in optimizing material properties for specific engineering applications. By selecting and designing appropriate grain structures, engineers can significantly improve material performance, offering an effective approach to increasingly satisfy demanding industrial requirements.

4. Summary and concluding remarks

In this study, the microscopic Hall–Petch relationship has been integrated into a rate-independent crystal plasticity framework to investigate size effects on the mechanical behavior of thin metal sheets. To this aim, polycrystalline unit cells with different grain sizes and distributions have been used to model these metal sheets. Periodic homogenization techniques have been employed to derive the macroscopic mechanical behavior from the properties of single crystal constituents. At the single crystal level, we adopted a finite strain elastoplastic framework with plastic flow modeled according to the classical Schmid law. The constitutive equations have been implemented within the ABAQUS/Standard finite element software via a UMAT subroutine. At the macroscopic scale, the ductility limit has been predicted by the Rice bifurcation criterion.

The results demonstrate that the proposed multiscale framework effectively captures the influence of grain size on macroscopic properties through the microscopic Hall–Petch relationship. The validation of the proposed size-dependent constitutive model, via comparisons between its numerical predictions and experimental data, confirms its capability of accurately capturing size effects, which emphasizes in particular the well-known ‘the smaller, the stronger’ phenomenon. The macroscopic strength is also found to increase with the unit cell thickness, emphasizing the role of structural dimensions in mechanical performance. Moreover, the study highlights the potential of gradient grain structures to overcome the traditional strength–ductility trade-off: such configurations significantly enhance both strength and ductility, offering a promising strategy for the design of advanced structural materials.

This study confirms the importance of controlling grain structure and size to enhance material properties, particularly in thin metal sheets. It also highlights the significant potential of gradient grain structures to revolutionize material design, providing a viable solution to the long-standing challenge of balancing strength and ductility in metallic materials.

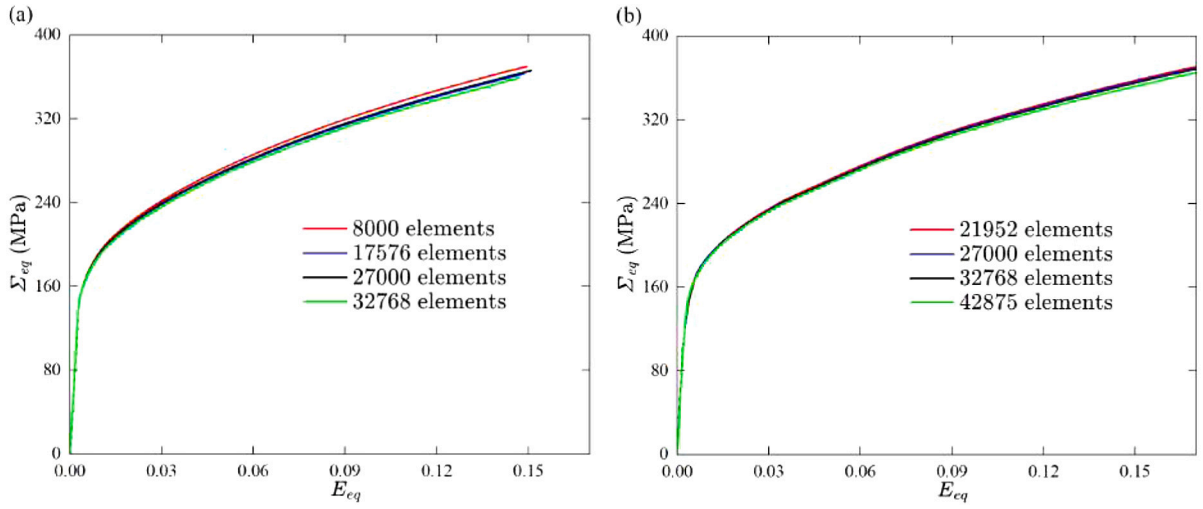

Fig. A.1. Mesh sensitivity analysis for the macroscopic stress–strain response under uniaxial tension. The simulations are performed on (a) the uniform grain structure and (b) the gradient grain structure, using several mesh densities. The results demonstrate that the macroscopic response is nearly insensitive to the number of finite elements in the tested range, confirming that the selected discretization of approximately 27,000 finite elements is sufficient to ensure a converged numerical solution.

CRediT authorship contribution statement

S. Zhou: Writing – original draft, Validation, Software, Methodology, Investigation, Data curation. **M. Ben Bettaieb:** Writing – review & editing, Supervision, Software, Methodology, Investigation. **F. Abed-Meraim:** Writing – original draft, Supervision, Methodology.

Declaration of competing interest

The authors declare that they have no known competing financial interests or personal relationships that could have appeared to influence the work reported in this paper.

Appendix A. Mesh sensitivity study

In this appendix, we perform a mesh sensitivity analysis to validate the adequacy of the number of finite elements used in our simulations. The unit cells depicted in Figs. 4(d) and 10(a) are selected as representative of uniform and gradient grain structures, and are successively discretized into four different finite element meshes. These analyses are conducted under uniaxial tension to examine the influence of mesh density on the macroscopic equivalent von Mises stress–strain response. The results presented in Fig. A.1 demonstrate that the macroscopic stress–strain curves are almost insensitive to the selected finite element discretization, among these four mesh refinements. Notably, the curves for finite element numbers from 17576 to 32768, for uniform grain structure, and from 21952 to 42875, for gradient grain structure, show nearly identical behavior. In the current investigation, unit cells with 27000 finite elements are used. This configuration effectively captures the mechanical behavior of the material, while preserving computational efficiency. Importantly, such a mesh refinement also helps prevent any distortion of the grain morphology in the gradient grain structure of the unit cell, which is crucial for accurate representation of material behavior in our models.

Appendix B. Comparison with experimental data of Liu et al. [100]

In this appendix, we have validated the accuracy of the proposed size-dependent constitutive model by comparing our numerical predictions with experimental data reported by Liu et al. [100]. For this purpose, unit cells with average grain size of 0.1266 mm, 0.10994 mm, and 0.09245 mm have been generated using the NEPER software [66], in accordance with the data provided by Liu et al. [100]. The unit cell volume is kept the same (i.e., $1.0 \times 1.0 \times 1.0$ mm^3) for these different average grain sizes. Fig. B.1 presents the corresponding unit cells, which comprise 875, 1338 and 2251 grains, respectively. Each unit cell is discretized using C3D8 finite elements, for a total of 27,000 finite elements. The adopted material parameters have been identified based on the experimental uniaxial tension response of the Inconel 718 sheet, which has an average grain size of $d_{av} = 0.1266$ mm and a random crystallographic texture. Fig. B.2(a) illustrates the accuracy of this identification procedure, and the identified parameters are provided in Table B.1.

In this validation study, each unit cell presented in Fig. B.1 has been assigned a random crystallographic texture and subjected to uniaxial tension loading. The corresponding macroscopic equivalent von Mises stress–strain curves predicted by the proposed model are shown in Fig. B.2(b), alongside the experimental results reported by Liu et al. [100]. As observed, the numerical predictions show good agreement with the experimental results. However, the flow stress predicted by the current size-dependent CPFE model tends to slightly overestimate the experimental values in the strain range $0.1 \leq E_{eq} \leq 0.25$. This minor discrepancy can be attributed to several factors, including the non-uniqueness of the fitted parameters. However, these material parameters have a significant impact on the numerical results, as demonstrated in Section 3.2.3 as well as by Zhou et al. [38]. Furthermore, other important elements, such as explicit grain boundary effects, real grain morphology, and initial crystallographic texture, were not taken into account in these specific validation simulations.

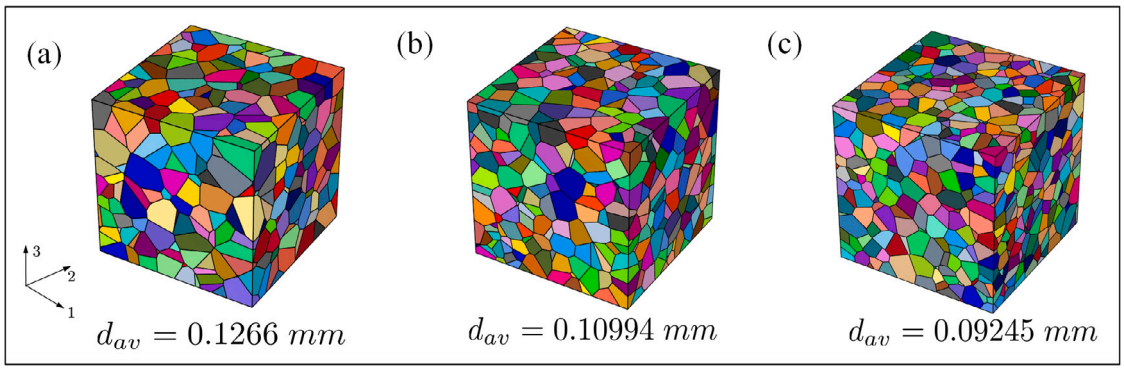

Fig. B.1. Representative Volume Elements (RVEs) generated for the validation study. The average grain sizes are chosen to match the experimental samples of Inconel 718 from Liu et al. [100]: (a) $d_{av} = 0.1266$ mm, (b) $d_{av} = 0.10994$ mm, and (c) $d_{av} = 0.09245$ mm.

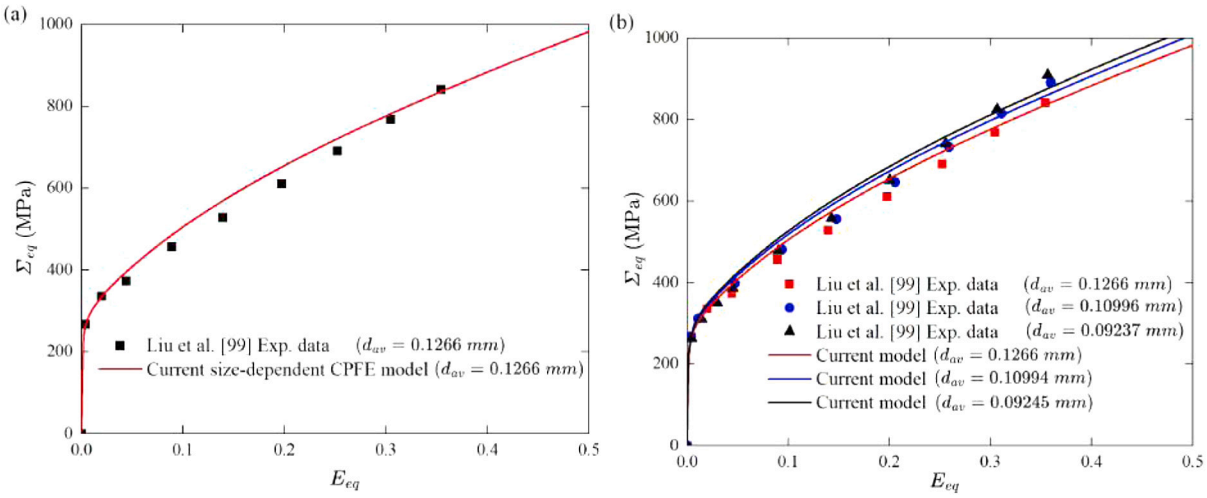

Fig. B.2. Validation of the size-dependent CPFE model against experimental uniaxial tension data for Inconel 718 from Liu et al. [100]. (a) Model Calibration: Material parameters have been identified by fitting the simulated stress–strain curve to the experimental data for the reference microstructure ($d_{av} = 0.1266$ mm). (b) Model Validation: Using the single set of calibrated parameters. The model successfully predicts the stress–strain responses for the two other grain sizes, confirming its predictive capability for the grain size effect.

Table B.1
Material parameters for the Inconel 718 sheet, fitted to the experimental data from Liu et al. [100].

	Notation	Value	Unit
Elasticity	E	200	GPa
	ν	0.3	–
	μ	76 923	MPa
Microscopic Hall–Petch constant	κ_{HP}	2.925	MPa $(\text{mm})^{1/2}$
Dislocation density-based hardening	τ_0	88	MPa
	h	1.0	–
	b	2.54×10^{-7}	mm
	A	0.4	–
	ρ_0	1.5×10^{8}	mm^{-2}
	y_c	1×10^{-6}	mm
	K	23.1	–

Data availability

No data was used for the research described in the article.

References

[1] Lu K. Making strong nanomaterials ductile with gradients: Microstructures that increase metal crystallite size from nanoscale with surface depth are both strong and ductile. Science 2014;345(6203):1455–6. http://dx.doi.org/10.1126/science.1255940.

[2] Chen S, Liu X, Liu L. Effects of grain size and heterogeneity on the mechanical behavior of foil rolling. Int J Mech Sci 2015;100:226–36. http://dx.doi.org/10.1016/j.ijmecsci.2015.07.003.

[3] Uchida M, Tsutsumi K, Sakamoto M, Kaneko Y. Characterization of size-affected non-uniform deformation of polycrystalline copper. Int J Mech Sci 2021;211:106760. http://dx.doi.org/10.1016/j.ijmecsci.2021.106760.

[4] Zhu Q, Luan D, Zhang L, Fan G, Qin H, Zhang P. Size effect on the forming limit of a nickel-based superalloy thin sheet at the mesoscopic scale. J Mater Res Technol 2023;26:8889–903. http://dx.doi.org/10.1016/j.jmrt.2023.09.204.

[5] Mehranpour MS, Sohrabi MJ, Kalhor A, Lee JH, Heydarinia A, Mirzadeh H, et al. Exceptional strength-ductility synergy in the novel metastable FeCoCrNiVSi high-entropy alloys via tuning the grain size dependency of the transformation-induced plasticity effect. Int J Plast 2024;182:104115. http://dx.doi.org/10.1016/j.ijplas.2024.104115.

[6] Peng SY, Tian YZ, Ni ZY, Lu S, Li S. Effect of grain size on the deformation mechanism and fracture behavior of a non-equiatomic CoCrNi alloy with low stacking fault energy. Int J Plast 2024;182. http://dx.doi.org/10.1016/j.ijplas.2024.104129.

[7] Zhang H, Shi J, Deng L, Tang X, Jin J, Zhang M, et al. Grain size effect on anisotropic acoustoplasticity of rolled α-Ti during ultrasonic vibration-assisted compression. Mater Sci Eng: A 2024;898:146407. http://dx.doi.org/10.1016/j.msea.2024.146407.

[8] Liu W, Wang R, Zhou H, Yao M, Sun W, Zhu Y, et al. Modeling of cryo-deformation based on grain size-dependent dislocation evolution. Int J Mech Sci 2025;285:109813. http://dx.doi.org/10.1016/j.ijmecsci.2024.109813.

[9] Su W, Wang M, Cheng Q, Yang B, Ye P, Lu X, et al. Probing the optimal grain size for the strength-ductility synergy in titanium via deformation dynamics. Mater Sci Eng: A 2025;924:147788. http://dx.doi.org/10.1016/j.msea.2025.147788.

[10] Wu H, Fan G. An overview of tailoring strain delocalization for strength-ductility synergy. Prog Mater Sci 2020;113:100675. http://dx.doi.org/10.1016/j.pmatsci.2020.100675.

[11] Li J, Weng GJ, Chen S, Wu X. On strain hardening mechanism in gradient nanostructures. Int J Plast 2017;88:89–107. http://dx.doi.org/10.1016/j.ijplas.2016.10.003.

[12] Li X, Lu L, Li J, Zhang X, Gao H. Mechanical properties and deformation mechanisms of gradient nanostructured metals and alloys. Nat Rev Mater 2020;5(9):706–23. http://dx.doi.org/10.1038/s41578-020-0212-2.

[13] Zhao F, Xie J, Zhu Y, Liu Q. A novel dynamic technique to form reverse grain size gradient microstructure in pure copper. Mater Lett 2021;291:129581. http://dx.doi.org/10.1016/j.matlet.2021.129581.

[14] Qin S, Yang M, Jiang P, Wang J, Wu X, Zhou H, et al. Designing structures with combined gradients of grain size and precipitation in high entropy alloys for simultaneous improvement of strength and ductility. Acta Mater 2022;230:117847. http://dx.doi.org/10.1016/j.actamat.2022.117847.

[15] Han J, Sun J, Song Y, Xu B, Yang Z, Xu S, et al. Achieving gradient heterogeneous structure in Mg alloy for excellent strength-ductility synergy. J Magnes Alloy 2023;11(7):2392–403. http://dx.doi.org/10.1016/j.jma.2021.09.021.

[16] Hall EO. The deformation and ageing of mild steel: III Discussion of results. Proc Phys Soc Sect B 1951;64(9):747–53. http://dx.doi.org/10.1088/0370-1301/64/9/303.

[17] Petch N. The cleavage strength of polycrystals. J Iron Steel Inst 1953;174:25–8.

[18] Zuev LB, Zarikovskaya NV, Fedosova MA. Plastic flow macrolocalization in aluminum and the Hall–Petch relation. Tech Phys 2010;55(9):1299–305. http://dx.doi.org/10.1134/S1063784210090112.

[19] Xu ZT, Peng LF, Fu MW, Lai XM. Size effect affected formability of sheet metals in micro/meso scale plastic deformation: Experiment and modeling. Int J Plast 2015;68:34–54. http://dx.doi.org/10.1016/j.ijplas.2014.11.002.

[20] Tvergaard V, Needleman A. Analysis of the cup-cone fracture in a round tensile bar. Acta Metall 1984;32(1):157–69. http://dx.doi.org/10.1016/0001-6160(84)90213-X.

[21] Thomason PF. A three-dimensional model for ductile fracture by the growth and coalescence of microvoids. Acta Metall 1985;33(6):1087–95. http://dx.doi.org/10.1016/0001-6160(85)90202-0.

[22] Xu ZT, Peng LF, Lai XM, Fu MW. Geometry and grain size effects on the forming limit of sheet metals in micro-scaled plastic deformation. Mater Sci Eng: A 2014;611:345–53. http://dx.doi.org/10.1016/j.msea.2014.05.060.

[23] Oyane M, Sato T, Okimoto K, Shima S. Criteria for ductile fracture and their applications. J Mech Work Technol 1980;4(1):65–81. http://dx.doi.org/10.1016/0378-3804(80)90006-6.

[24] Holmberg S, Enquist B, Thilderkvist P. Evaluation of sheet metal formability by tensile tests. J Mater Process Technol 2004;145(1):72–83. http://dx.doi.org/10.1016/j.jmatprotec.2003.07.004.

[25] Wilson DV, Mirshams AR, Roberts WT. An experimental study of the effect of sheet thickness and grain size on limit-strains in biaxial stretching. Int J Mech Sci 1983;25(12):859–70. http://dx.doi.org/10.1016/0020-7403(83)90017-6.

[26] Berbenni S, Favier V, Berveiller M. Impact of the grain size distribution on the yield stress of heterogeneous materials. Int J Plast 2007;23(1):114–42. http://dx.doi.org/10.1016/j.ijplas.2006.03.004.

[27] Nicaise N, Berbenni S, Wagner F, Berveiller M, Lemoine X. Coupled effects of grain size distributions and crystallographic textures on the plastic behaviour of if steels. Int J Plast 2011;27(2):232–49. http://dx.doi.org/10.1016/j.ijplas.2010.05.001.

[28] Franz G, Abed-Meraim F, Berveiller M. Effect of microstructural and morphological parameters on the formability of BCC metal sheets. Steel Res Int 2014;85(6):980–7. http://dx.doi.org/10.1002/srin.201300166.

[29] Kocks U. Laws for work-hardening and low-temperature creep. J Eng Mater Technol 1976;98(1):76–85. http://dx.doi.org/10.1115/1.3443340.

[30] Haouala S, Segurado J, LLorca J. An analysis of the influence of grain size on the strength of FCC polycrystals by means of computational homogenization. Acta Mater 2018;148:72–85. http://dx.doi.org/10.1016/j.actamat.2018.01.024, arXiv:1801.05155.

[31] Bong HJ, Lee J. Crystal plasticity finite element-Marciniak-Kuczynski approach with surface roughening effect in predicting formability of ultra-thin ferritic stainless steel sheets. Int J Mech Sci 2021;191:106066. http://dx.doi.org/10.1016/j.ijmecsci.2020.106066.

[32] Tran MT, Wang H, Lee HW, Kim DK. Crystal plasticity finite element analysis of size effect on the formability of ultra-thin ferritic stainless steel sheet for fuel cell bipolar plate. Int J Plast 2022;154:103298. http://dx.doi.org/10.1016/j.ijplas.2022.103298.

[33] Zhu JC, Ben Bettaieb M, Zhou S, Abed-Meraim F. Ductility limit prediction for polycrystalline aggregates using a CPFEM-based multiscale framework. Int J Plast 2023;167:103671. http://dx.doi.org/10.1016/j.ijplas.2023.103671.

[34] Mikula J, Vastola G, Zhang YW. Dual-phase polycrystalline crystal plasticity model revealing the relationship between microstructural characteristics and mechanical properties in additively manufactured maraging steel. Int J Plast 2024;180:104058. http://dx.doi.org/10.1016/j.ijplas.2024.104058.

[35] Wang M, Wang X, Sun P, Li H, Liu Z, Yang G, et al. Multi-scale investigation on grain size effect of a powder metallurgy Ni-based superalloy based on simulation and experimental characterization. Intermetallics 2024;173:108429. http://dx.doi.org/10.1016/j.intermet.2024.108429.

[36] Yan B, Lin P, Yang L, Jiang S, Sun D, Feng H, et al. Revealing size effect for plastic deformation of nanocrystalline NiTi SMA at moderate temperature by combining CPFEM with experiment. J Mater Res Technol 2024;30:7869–84. http://dx.doi.org/10.1016/j.jmrt.2024.05.169.

[37] Sun L, Xu Z, Wang J, Peng L, Lai X, Fu MW. Coupled cellular automata-crystal plasticity modeling of microstructure-sensitive damage and fracture behaviors in deformation of α-titanium sheets affected by grain size. Int J Plast 2024;182. http://dx.doi.org/10.1016/j.ijplas.2024.104138.

[38] Zhou S, Ben Bettaieb M, Abed-Meraim F. A physically-based mixed hardening model for the prediction of the ductility limits of thin metal sheets using a CPFE approach. Int J Plast 2024;176:103946. http://dx.doi.org/10.1016/j.ijplas.2024.103946.

[39] Zhou S, Ben Bettaieb M, Abed-Meraim F. Investigation of the effect of morphological and crystallographic textures on the ductility limits of thin metal sheets using a CPFEM-based approach. Eur J Mech A Solids 2024;106. http://dx.doi.org/10.1016/j.euromechsol.2024.105293.

[40] Zhou S, Ben Bettaieb M, Abed-Meraim F. A crystal plasticity-damage coupled finite element framework for predicting mechanical behavior and ductility limits of thin metal sheets. Int J Plast 2025;187:104267. http://dx.doi.org/10.1016/j.ijplas.2025.104267.

[41] Taherijam M, Abdolvand H. Hydrogen and hydride induced stress localization in single phase HCP and dual phase HCP-BCC alloys. Int J Plast 2025;189:1–28. http://dx.doi.org/10.1016/j.ijplas.2025.104325.

[42] An W, Yang JP, Liu CZ, Xiong QL. Effect of twinning on shear localization of Al0.1CoCrFeNi high entropy alloy at high strain rates: Experiment and crystal plasticity modeling. Int J Plast 2025;189:104339. http://dx.doi.org/10.1016/j.ijplas.2025.104339.

[43] Paramatmuni C, Kanjarla AK. A crystal plasticity FFT based study of deformation twinning, anisotropy and micromechanics in HCP materials: Application to AZ31 alloy. Int J Plast 2019;113:269–90. http://dx.doi.org/10.1016/j.ijplas.2018.10.007.

[44] Roters F, Diehl M, Shanthraj P, Eisenlohr P, Reuber C, Wong SL, et al. DAMASK - the Düsseldorf Advanced Material Simulation Kit for modeling multi-physics crystal plasticity, thermal, and damage phenomena from the single crystal up to the component scale. Comput Mater Sci 2019;158:420–78. http://dx.doi.org/10.1016/j.commatsci.2018.04.030.

[45] Berbenni S, Taupin V, Lebensohn RA. A fast Fourier transform-based mesoscale field dislocation mechanics study of grain size effects and reversible plasticity in polycrystals. J Mech Phys Solids 2020;135:1–23. http://dx.doi.org/10.1016/j.jmps.2019.103808.

[46] Haouala S, Lucarini S, LLorca J, Segurado J. Simulation of the Hall–Petch effect in FCC polycrystals by means of strain gradient crystal plasticity and FFT homogenization. J Mech Phys Solids 2020;134. http://dx.doi.org/10.1016/j.jmps.2019.103755.

[47] Flipon B, Keller C, Quey R, Barbe F. A full-field crystal-plasticity analysis of bimodal polycrystals. Int J Solids Struct 2020;184:178–92. http://dx.doi.org/10.1016/j.ijsolstr.2019.02.005.

[48] Motaman SAH, Roters F, Haase C. Anisotropic polycrystal plasticity due to microstructural heterogeneity: A multi-scale experimental and numerical study on additively manufactured metallic materials. Acta Mater 2020;185:340–69. http://dx.doi.org/10.1016/j.actamat.2019.12.003.

[49] Wang C, Wu H, Wang X, Wang C, Wang L. Numerical study of microscale laser bulging based on crystal plasticity. Int J Mech Sci 2020;177:105553. http://dx.doi.org/10.1016/j.ijmecsci.2020.105553.

[50] Fischer T, Hitzler L, Werner E. Morphological and crystallographic effects in the laser powder-bed fused stainless steel microstructure. Crystals 2021;11(6):1–19. http://dx.doi.org/10.3390/cryst11060672.

[51] Agius D, Kareer A, Mamun AA, Truman C, Collins DM, Mostafavi M, et al. A crystal plasticity model that accounts for grain size effects and slip system interactions on the deformation of austenitic stainless steels. Int J Plast 2022;152:103249. http://dx.doi.org/10.1016/j.ijplas.2022.103249.

[52] Gu S, Zhao J, Ma T, Xu T, Yu B. Modeling and analysis of grain morphology effects on deformation response based on crystal plasticity finite element method. Mater Und Werkst 2022;53(7):770–80. http://dx.doi.org/10.1002/mawe.202100172.

[53] Tong X, Li Y, Fu MW. Modelling of grain size effects in progressive microforming using CPFEM. Int J Mech Sci 2024;267. http://dx.doi.org/10.1016/j.ijmecsci.2024.108971.

[54] Lakshmanan A, Andani MT, Yaghoobi M, Allison J, Misra A, Sundararaghavan V. A combined experimental and crystal plasticity study of grain size effects in magnesium alloys. J Magnes Alloy 2023;11:4445–67. http://dx.doi.org/10.1016/j.jma.2023.05.008.

[55] Chandra S, Samal MK, Naveen Kumar N, Chavan VM. Atomistically informed crystal plasticity analysis of deformation behavior of alloy 690 including grain boundary effects. Materialia 2021;16:101053. http://dx.doi.org/10.1016/j.mtla.2021.101053.

[56] Chandra S, Samal MK, Kumar NN, Chavan VM. Simulation of Hall–Petch effect in alloy 690 using crystal plasticity model considering effect of grain boundaries. Mater Lett 2021;297:129915. http://dx.doi.org/10.1016/j.matlet.2021.129915.

[57] Li K, Tang B, Zhang H, Zhang M, Chu Y, Zhang W, et al. Crystal plasticity framework related to size effect: From single crystal parameters to polycrystalline mechanical properties. Mater Sci Eng: A 2024;907:146747. http://dx.doi.org/10.1016/j.msea.2024.146747.

[58] Jiang M, Fan Z, Kruch S, Devincre B. Grain size effect of FCC polycrystal: A new CPFEM approach based on surface geometrically necessary dislocations. Int J Plast 2022;150:103181. http://dx.doi.org/10.1016/j.ijplas.2021.103181.

[59] Amouzou-Adoun YA, Jebahi M, Fivel M, Forest S, Lecomte JS, Schuman C, et al. On elastic gaps in strain gradient plasticity: 3D discrete dislocation dynamics investigation. Acta Mater 2023;252:118920. http://dx.doi.org/10.1016/j.actamat.2023.118920.

[60] Zhang X, Zhao J, Kang G, Zaiser M. Geometrically necessary dislocations and related kinematic hardening in gradient grained materials: A nonlocal crystal plasticity study. Int J Plast 2023;163:103553. http://dx.doi.org/10.1016/j.ijplas.2023.103553.

[61] Amouzou-Adoun YA, Jebahi M, Forest S, Fivel M. Advanced modeling of higher-order kinematic hardening in strain gradient crystal plasticity based on discrete dislocation dynamics. J Mech Phys Solids 2024;193. http://dx.doi.org/10.1016/j.jmps.2024.105875.

[62] Liu C-Z, Xiong Q-L, Wen A. Shear localization in gradient high-entropy alloy at high strain rates: Crystal plasticity modeling. Extrem Mech Lett 2024;70:102194. http://dx.doi.org/10.1016/j.eml.2024.102194.

[63] Lame Jouybari A, El Shawish S, Cizelj L. Fast Fourier transform approach to Strain Gradient Crystal Plasticity: Regularization of strain localization and size effect. Int J Plast 2024;183:104153. http://dx.doi.org/10.1016/j.ijplas.2024.104153.

[64] Akpama HK, Ben Bettaieb M, Abed-Meraim F. Numerical integration of rate-independent BCC single crystal plasticity models: comparative study of two classes of numerical algorithms. Internat J Numer Methods Engrg 2016;108(5):363–422. http://dx.doi.org/10.1002/nme.5215.

[65] Hollister SJ, Kikuchi N. A comparison of homogenization and standard mechanics analyses for periodic porous composites. Comput Mech 1992;10(2):73–95. http://dx.doi.org/10.1007/BF00369853.

[66] Quey R, Dawson PR, Barbe F. Large-scale 3D random polycrystals for the finite element method: Generation, meshing and remeshing. Comput Methods Appl Mech Engrg 2011;200(17):1729–45. http://dx.doi.org/10.1016/j.cma.2011.01.002.

[67] Geuzaine C, Remacle J-F. Gmsh: A 3-D finite element mesh generator with built-in pre- and post-processing facilities. Internat J Numer Methods Engrg 2009;79(11):1309–31. http://dx.doi.org/10.1002/nme.2579.

[68] Beausir B, Fundenberger J-J. Analysis tools for electron and X-ray diffraction, ATEX - software, . Univ. lorraine - metz. 2017, www.atex-software.eu.

[69] Lejeunes S, Bourgeois S. Une toolbox abaqus pour le calcul de propriétés effectives de milieux hétérogènes. In: 10e Colloque National en Calcul des Structures, Giens, France. 2011, p. 1–9.

[70] Van Der Sluis O, Schreurs PJ, Brekelmans WA, Meijer HE. Overall behaviour of heterogeneous elastoviscoplastic materials: Effect of microstructural modelling. Mech Mater 2000;32(8):449–62. http://dx.doi.org/10.1016/S0167-6636(00)00019-3.

[71] Saai A, Dumoulin S, Hopperstad OS, Lademo OG. Simulation of yield surfaces for aluminium sheets with rolling and recrystallization textures. Comput Mater Sci 2013;67:424–33. http://dx.doi.org/10.1016/j.commatsci.2012.08.015.

[72] Bong HJ, Lee J, Hu X, Sun X, Lee MG. Predicting forming limit diagrams for magnesium alloys using crystal plasticity finite elements. Int J Plast 2020;126:102630. http://dx.doi.org/10.1016/j.ijplas.2019.11.009.

[73] Agaram S, Kanjarla AK, Bhuvaraghan B, Srinivasan SM. Dislocation density based crystal plasticity model incorporating the effect of precipitates in IN718 under monotonic and cyclic deformation. Int J Plast 2021;141:102990. http://dx.doi.org/10.1016/j.ijplas.2021.102990.

[74] Isavand S, Kardan-Halvaei M, Assempour A. Crystal plasticity modeling and experimental characterization of strain localization and forming limits in ferrite-pearlite steels. Int J Solids Struct 2021;233:111205. http://dx.doi.org/10.1016/j.ijsolstr.2021.111205.

[75] Singh L, Ha S, Vohra S, Sharma M. Computational homogenization based crystal plasticity investigation of deformation behavior of AA2024-T3 alloy at different strain rates. Multidiscip Model Mater Struct 2023;19(3):420–40. http://dx.doi.org/10.1108/MMMS-10-2022-0236.

[76] Quey R, Dawson P, Barbe F. Large-scale 3D random polycrystals for the finite element method: Generation, meshing and remeshing. Comput Methods Appl Mech Engrg 2011;200(17–20):1729–45. http://dx.doi.org/10.1016/j.cma.2011.01.002.

[77] Kanit T, Forest S, Mounoury V, Jeulin D. Determination of the size of the representative volume element for random composites: statistical and numerical approach. Int J Solids Struct 2003;40(13–14):3647–79. http://dx.doi.org/10.1016/S0020-7683(03)00143-4.

[78] Barbe F, Forest S, Cailletaud G. Intergranular and intragranular behavior of polycrystalline aggregates.Part 2: Results. Int J Plast 2001;17(4):537–63. http://dx.doi.org/10.1016/S0749-6419(00)00062-0.

[79] Lee S, Lebensohn R, Rollet A. Modeling the viscoplastic micromechanical response of two-phase materials using fast Fourier transforms. Int J Plast 2011;27(5):707–27. http://dx.doi.org/10.1016/j.ijplas.2010.09.002.

[80] Ben Bettaieb M, Débordes O, Dogui A, Duchêne L, Keller C. On the numerical integration of rate independent single crystal behavior at large strain. Int J Plast 2012;32–33:184–217. http://dx.doi.org/10.1016/j.ijplas.2011.10.010.

[81] Fischer A. Solution of monotone complementarity problems with locally Lipschitzian functions. Math Program Ser B 1997;76(3):513–32. http://dx.doi.org/10.1007/BF02614396.

[82] Akpama HK, Ben Bettaieb M, Abed-Meraim F. Localized necking predictions based on rate-independent self-consistent polycrystal plasticity: Bifurcation analysis versus imperfection approach. Int J Plast 2017;91:205–37. http://dx.doi.org/10.1016/j.ijplas.2017.02.001.

[83] Anand L, Kothari M. A computational procedure for rate-independent crystal plasticity. J Mech Phys Solids 1996;44(4):525–58. http://dx.doi.org/10.1016/0022-5096(96)00001-4.

[84] Rice J. The localization of plastic deformation. In: 14th international congress of theoretical and applied mechanics. 1976, p. 207–20.

[85] Marciniak Z, Kuczyński K. Limit strains in the processes of stretch-forming sheet metal. Int J Mech Sci 1967;9(9):609–20. http://dx.doi.org/10.1016/0020-7403(67)90066-5.

[86] Miehe C. Computational micro-to-macro transitions for discretized micro-structures of heterogeneous materials at finite strains based on the minimization of averaged incremental energy. Comput Methods Appl Mech Engrg 2003;192(5):559–91. http://dx.doi.org/10.1016/S0045-7825(02)00564-9.

[87] Zhu JC, Ben Bettaieb M, Abed-Meraim F. Comparative study of three techniques for the computation of the macroscopic tangent moduli by periodic homogenization scheme. Eng Comput 2022;38:1365–94. http://dx.doi.org/10.1007/s00366-020-01091-y.

[88] Yoshida K, Kuroda M. Comparison of bifurcation and imperfection analyses of localized necking in rate-independent polycrystalline sheets. Int J Solids Struct 2012;49(15–16):2073–84. http://dx.doi.org/10.1016/j.ijsolstr.2012.04.010.

[89] Bratov V, Borodin EN. Comparison of dislocation density based approaches for prediction of defect structure evolution in aluminium and copper processed by ECAP. Mater Sci Eng: A 2015;631:10–7. http://dx.doi.org/10.1016/j.msea.2015.02.019.

[90] Banerjee B, Bhawalkar AS. An extended mechanical threshold stress plasticity model: Modeling 6061-T9 aluminum alloy. J Mech Mater Struct 2008;3(3):391–424. http://dx.doi.org/10.2140/jomms.2008.3.391.

[91] Meng F. Simulations à l'échelle mesoscopic du comportement en fatigue de métaux CFC (Ph.D. thesis), Université Grenoble Alpes; 2020, URL https://tel.archives-ouvertes.fr/tel-03116144.

[92] Hug E, Keller C. Intrinsic effects due to the reduction of thickness on the mechanical behavior of nickel polycrystals. Met Mater Trans A: Phys Met Mater Sci 2010;41(10):2498–506. http://dx.doi.org/10.1007/s11661-010-0286-3.

[93] Mahabunphachai S, Koç M. Investigation of size effects on material behavior of thin sheet metals using hydraulic bulge testing at micro/meso-scales. Int J Mach Tools Manuf 2008;48(9):1014–29. http://dx.doi.org/10.1016/j.ijmachtools.2008.01.006.

[94] Lyu H, Zhang Y, Li H. The effect of grain size gradient on plastic deformation of gradient aluminum. Met Mater Trans A: Phys Met Mater Sci 2022;53(9):3428–40. http://dx.doi.org/10.1007/s11661-022-06758-3.

[95] Wang Y, Yang G, Wang W, Wang X, Li Q, Wei Y. Optimal stress and deformation partition in gradient materials for better strength and tensile ductility: A numerical investigation. Sci Rep 2017;7(1):1–8. http://dx.doi.org/10.1038/s41598-017-10941-7.

[96] Yoshida K, Brenner R, Bacroix B, Bouvier S. Effect of regularization of Schmid law on self-consistent estimates for rate-independent plasticity of polycrystals. Eur J Mech A Solids 2009;28(5):905–15. http://dx.doi.org/10.1016/j.euromechsol.2009.05.001.

[97] Ben Bettaieb M, Abed-Meraim F. Investigation of localized necking in substrate-supported metal layers: Comparison of bifurcation and imperfection analyses. Int J Plast 2015;65:168–90. http://dx.doi.org/10.1016/j.ijplas.2014.09.003.

[98] Ben Bettaieb M, Abed-Meraim F. Theoretical and numerical investigation of the impact of out-of-plane compressive stress on sheet metal formability. Int J Mech Sci 2017;130:244–57. http://dx.doi.org/10.1016/j.ijmecsci.2017.05.046.

[99] Lu X, Zhao J, Wang Z, Gan B, Zhao J, Kang G, et al. Crystal plasticity finite element analysis of gradient nanostructured TWIP steel. Int J Plast 2020;130:102703. http://dx.doi.org/10.1016/j.ijplas.2020.102703.

[100] Liu BB, Han JQ, Zhao R, Liu W, Wan M. Grain size effect on fracture behavior of the axis-tensile test of inconel 718 sheet. High Temp Mater Process 2016;35(10):989–98. http://dx.doi.org/10.1515/htmp-2015-0102.